



Large-scale features of Last Interglacial climate: Results from evaluating the *lig127k* simulations for CMIP6-PMIP4

Bette L. Otto-Bliesner¹, Esther C. Brady¹, Anni Zhao², Chris Brierley², Yarrow Axford³, Emilie
5 Capron⁴, Aline Govin⁵, Jeremy Hoffman^{6,7}, Elizabeth Isaacs², Masa Kageyama⁵, Paolo
Scussolini⁸, Polychronis C. Tzedakis², Charlie Williams⁹, Eric Wolff¹⁰, Ayako Abe-Ouchi¹¹,
Pascale Braconnot⁵, Silvana Ramos Buarque¹², Jian Cao¹³, Anne de Vernal¹⁴, Maria Vittoria
Guarino¹⁵, Chuncheng Guo¹⁶, Allegra N. LeGrande¹⁷, Gerrit Lohmann¹⁸, Katrin Meissner¹⁹,
10 Laurie Menviel¹⁹, Kerim Nisancioglu^{20,21}, Ryouta O'ishi¹¹, David Salas Y Melia¹², Xiaoxu Shi¹⁸,
Marie Sicard⁵, Louise Sime¹⁵, Robert Tomas¹, Evgeny Volodin²², Nicolas Yeung¹⁹, Qiong
Zhang²³, Zhonghi Zhang¹⁶, Weipeng Zheng²⁴

¹Climate and Global Dynamics Laboratory, National Center for Atmospheric Research, Boulder, 80305, USA

15 ²University College London, Department of Geography, WC1E 6BT, UK

³Department of Earth & Planetary Sciences, Northwestern University, Illinois, USA

⁴Physics of Ice, Climate and Earth, Niels Bohr Institute, University of Copenhagen, Copenhagen, 2200, Denmark.

⁵LSCE-IPSL, Laboratoire des Sciences du Climat et de l'Environnement (CEA-CNRS-UVSQ), University Paris-Saclay, Gif sur Yvette, 91190, France

20 ⁶Science Museum of Virginia, Richmond, Virginia, 23220, USA

⁷Center for Environmental Studies, Virginia Commonwealth University, Richmond, VA, 23220, USA

⁸Earth and Climate Group, Vrije Universiteit, Amsterdam, the Netherlands

⁹School of Geographical Sciences, University of Bristol, Bristol, UK

¹⁰Department of Earth Sciences, University of Cambridge, Cambridge, CB2 3EQ, United Kingdom.

25 ¹¹Atmosphere Ocean Research Institute, University of Tokyo, 5-1-5, Kashiwanoha, Kashiwa-shi, Chiba 277-8564, Japan

¹²CNRM (Centre National de Recherches Météorologiques), Université de Toulouse, Météo-France, CNRS (Centre National de la Recherche Scientifique), Toulouse, France

¹³Earth System Modeling Center, Nanjing University of Information Science and Technology, Nanjing, 210044, China

30 ¹⁴Département des sciences de la Terre et de l'atmosphère, Université du Québec, Montreal, Canada

¹⁵British Antarctic Survey, High Cross, Madingley Road, Cambridge, CB3 0ET, UK

¹⁶NORCE Norwegian Research Centre, Bjerknes Centre for Climate Research, Bergen 5007, Norway

¹⁷NASA Goddard Institute for Space Studies and Center for Climate Systems Research, Columbia University, New York City, USA

35 ¹⁸Alfred Wegener Institute - Helmholtz Centre for Polar and Marine Research, Bussestr. 24, 27570 Bremerhaven, Germany

¹⁹Climate Change Research Centre, The University of New South Wales, Sydney, NSW 2052, Australia

²⁰Department of Earth Science, University of Bergen, Bjerknes Centre for Climate Research, Allégaten 41, 5007, Bergen, Norway

40 ²¹Centre for Earth Evolution and Dynamics, University of Oslo, Oslo, Norway

²²State Key Laboratory of Numerical Modeling for Atmospheric Sciences and Geophysical Fluid Dynamics, Institute of Atmospheric Physics, Chinese Academy of Sciences, 100029, Beijing, China

²³Department of Physical Geography and Bolin Centre for Climate Research, Stockholm University, Stockholm, 10691, Sweden

45 ²⁴LASG, Institute of Atmospheric Physics, Chinese Academy of Sciences, Beijing 100029, China

Correspondence to: Bette Otto-Bliesner (ottobli@ucar.edu)

50 **Abstract.** The modeling of paleoclimate, using physically based tools, is increasingly seen as a strong out-of-sample test of the models that are used for the projection of future climate changes. New to CMIP6 is the Tier 1 *lig127k*



experiment, designed to address the climate responses to stronger orbital forcing than the *midHolocene* experiment, using the same state-of-the-art models and following a common experimental protocol. We present a multi-model ensemble of 17 climate models, all of which (except for two) have also completed the CMIP6 DECK experiments.

55 The Equilibrium Climate Sensitivity (ECS) of these models varies from 2.1 to 5.3°C. The seasonal character of the insolation anomalies results in strong warming over the Northern Hemisphere (NH) continents in the *lig127k* ensemble as compared to the *piControl* in June-July-August and a much-reduced minimum (August-September) summer sea ice extent in the Arctic. The multi-model results indicate enhanced summer monsoonal precipitation and areal extent in the Northern Hemisphere and reductions in the Southern Hemisphere. These responses are greater in

60 the *lig127k* than *midHolocene* simulations as expected from the larger insolation anomalies at 127 ka than 6 ka.

New syntheses for surface temperature and precipitation, targeted for 127ka, have been developed for comparison to the multi-model ensemble. The *lig127k* model ensemble and data reconstructions are in good agreement for summer temperature anomalies over Canada, Scandinavia, and the North Atlantic and precipitation over the Northern Hemisphere continents. The model-data comparisons and mismatches point to further study of the sensitivity of the

65 simulations to uncertainties in the specified boundary conditions and of the uncertainties and sparse coverage in current proxy reconstructions.

The CMIP6-PMIP4 *lig127k* simulations, in combination with the proxy record, have potential implications for confidence in future projections of monsoons, surface temperature, Arctic sea ice, and the stability of the Greenland ice sheet.

70

1 Introduction

Quaternary interglacials can be thought of as natural experiments to study the response of the climate system to variations in forcings and feedbacks (Tzedakis et al., 2009). The current interglacial (Holocene, the last 11,600 years) and the last interglacial (LIG; ~129,000-116,000 years before present) are well represented in the geological

75 record and provide an opportunity to study the impact of differences in orbital forcing. Two interglacial timeslices, the mid-Holocene (*midHolocene* or MH, ~6,000 years before present) and the early part of the LIG (*lig127k*; 127,000 thousand years before present), are included as Tier 1 simulations in the Coupled Model Intercomparison Project (CMIP6) and Paleoclimate Modeling Intercomparison Project (PMIP4). These equilibrium simulations are designed to examine the impact of changes in the Earth's orbit on the latitudinal and seasonal distribution of incoming solar

80 radiation (insolation) at times when atmospheric greenhouse gas levels were similar to those of the preindustrial period and the continental configurations were also very similar to modern. They test our understanding of the interplay between radiative forcing and atmospheric circulation, and the connections between large-scale and regional climate changes giving rise to phenomena such high-latitude amplification in temperature changes, and responses of the monsoons, as compared to today.

85 The modeling of paleoclimate, using physically based tools, has long been used to understand and explain past environmental and climate changes (Kutzbach and Otto-Bliesner, 1982; Braconnot et al., 2012; Harrison et al., 2015; Schmidt et al., 2014). In the first phase of PMIP, the MH and the Last Glacial Maximum (LGM, ~21,000 years ago)



90 were identified as important time periods to compare data reconstructions and model simulations (Joussaume et al.,
1999; Braconnot et al., 2000). A novel aspect in CMIP5 is having the same models and configurations used in the
paleo-climate simulations as with the transient 20th century and future simulations, implying that consistency – both
in the overall forcings and in how they are imposed – with those other experiments is a very strong requirement. In
addition to MH and LGM experiments, CMIP5 and PMIP3 included coordinated protocols for Last Millennium (LM,
850-1850 CE) and the mid-Pliocene Warm Period (mPWP, 3.3-3.0 million years ago) experiments.

95

The LIG is recognized as an important period for testing our knowledge of climate and climate-ice sheet interactions
to forcing in warm climate states. Although the LIG was discussed in the First Assessment Report of the IPCC
(Folland et al., 1990), it gained more prominence in the IPCC Fourth and Fifth Assessments (AR4 and AR5) (Jansen
et al., 2007; Masson-Delmotte et al., 2013). Evidence in the geologic record indicate a warm Arctic (Turney et al.,
100 2010) and a global mean sea level highstand at least 5 m higher (but probably no more than 10 m higher) than present
for several thousand years (Dutton et al., 2015) during the LIG. The ensemble of LIG simulations examined in the
AR5 (Masson-Delmotte et al., 2013) was not wholly consistent; the orbital forcing and GHG concentrations varied
between the simulations. While it had been suggested that differences in regional temperatures between models might
reflect differences in cryosphere feedback strength (Yin and Berger, 2012; Otto-Bliesner et al., 2013) or differences
105 in the simulation of the Atlantic Meridional Overturning Circulation (AMOC) (Bakker et al., 2013), differences
between models could also have arisen because of differences in the experimental protocols. Furthermore, the LIG
simulations were mostly made with older and/or lower-resolution versions of the models than were used for future
projections, making it more difficult to use the results to assess model reliability (Lunt et al., 2013).

110 For the first time the LIG has been designated as a CMIP6 simulation, setting a common experimental protocol and
asking modeling groups to run with the same model and at the same resolution as the DECK simulations (Otto-
Bliesner et al., 2016). At the PAGES QUIGS workshop in Cambridge in 2015, the community identified the 127ka
time slice for the CMIP6-PMIP4 LIG experiment for several reasons: large Northern Hemisphere seasonal insolation
anomalies, no (or little) remnants of the North American and Eurasian ice sheets, and sufficient time to allow for
115 dating uncertainties to minimize the imprint of the previous deglaciation and the Heinrich 11 (H11) meltwater event
(Marino et al., 2015). The Tier 1 *lig127k* experiment addresses the climate responses to stronger orbital forcing,
relative to the *midHolocene*. It also provides a basis to address the linkages between ice sheets and climate change in
collaboration with the Ice Sheet Model Intercomparison Project for CMIP6 (ISMIP6) (Nowicki et al., 2016).

120 In this paper, we provide a brief review of the experimental design of the *lig127k* simulation (Otto-Bliesner et al.,
2016), an overview of the models included in the ensemble, and details of the new syntheses of surface temperature
and precipitation proxies, targeted for 127 ka, developed for this project. We present the multi-model ensemble mean
and model spread for surface temperature, precipitation, and sea ice responses as compared to the CMIP6 DECK
piControl simulations from the same models and as compared to the data reconstructions. We also explore
125 differences in the responses of surface temperature, monsoon precipitation, and Arctic sea to the different magnitudes



and seasonal character of the insolation anomalies at 127 ka versus 6 ka. We conclude with a discussion of possible reasons for the model-data differences.

2 Methods

2.1 Experimental design

130 The CMIP DECK *piControl* for 1850 CE (see Eyring et al. 2016 for description of this experiment) is the reference simulation to which the *lig127k* paleo-experiment is compared. The modeling groups were asked to use the same model components and follow the same protocols for implementing external forcings as are used in the *piControl*. The boundary conditions for the *lig127k*, and *piControl* experiments are given in Table 1, and more detailed information is given below.

135 Earth's orbital parameters (eccentricity, longitude of perihelion, and obliquity) are prescribed following Berger and Loutre (1991). The DECK *piControl* simulations use the orbital parameters appropriate for 1850 CE (Table 1, Fig. 1) (Eyring et al., 2016), when perihelion occurs close to the boreal winter solstice. The orbit at 127 ka is characterized by larger eccentricity than at 1850 CE., with perihelion occurring close to the boreal summer solstice (Table 1, Fig. 1). The tilt of the Earth's axis was maximal at 131 ka and remained higher than in 1850 CE through 125 ka; obliquity 140 at 127 ka was 24.04° (Table 1). The solar constant for the *lig127k* simulations is prescribed to be the same as in the DECK *piControl* simulation, which is fixed at the mean value for the first two solar cycles of the historical simulation (i.e. 1850-1871) (Eyring et al., 2016).

145 The orbital parameters affect the seasonal and latitudinal distribution and magnitude of solar energy received at the top of the atmosphere, resulting in large positive insolation anomalies during boreal summer at 127 ka as compared to 1850 CE (Fig. 1). Positive insolation anomalies are present from April to September and from 60°S to 90°N. These anomalies peak at over 70 W m⁻² in June at 90°N. Insolation in the Arctic (defined here as 60-90°N) is more than 10% greater at 127 ka than 1850 CE during May through early August. The higher obliquity at 127 ka contributes to 150 a small but positive annual insolation anomaly compared to preindustrial at high latitudes in both hemispheres. The global difference in annual insolation forcing between the *lig127k* and *piControl* experiments is negligible.

Ice-core records from Antarctica provide measurements of the well-mixed GHGs: CO₂, CH₄, and N₂O. By 127 ka, the concentrations of atmospheric CO₂ and CH₄ had increased from their respective levels during the previous glacial 155 period, to values comparable to, albeit somewhat lower than, preindustrial levels (Table 1).

Natural aerosols show large variations on glacial-interglacial time scales, with low aerosol loadings during interglacials compared to glacials, and during the peak of the interglacials compared to present day (Albani et al., 2015; deMenocal et al., 2000; Kohfeld and Harrison, 2000). Modeling groups were asked to implement changes in 160 atmospheric dust aerosol in their *lig127k* simulations following the treatment used for their DECK *piControl* simulations (see Table 2 for details). The background volcanic stratospheric aerosol used in the CMIP6 DECK



piControl was to be used for the *lig127k* simulation. Other aerosols included in the DECK *piControl* simulations should similarly be included in the *lig127k* simulations.

165 There is evidence for changes in vegetation distribution during the LIG (e.g. LIGA Members, 1991; CAPE, 2006; Larrasoana, 2013). However, there is insufficient data coverage for many regions to be able to produce reliable global vegetation maps. Furthermore, given the very different levels of complexity in the treatment of vegetation properties in the current generation of climate models, paleo-observations do not provide sufficient information to constrain their behavior in a comparable way. The treatment of natural vegetation in the *lig127k* simulations was therefore to
170 be the same as in the DECK *piControl* simulation. Accordingly, depending on what was done in the DECK *piControl* simulation, vegetation could either be prescribed to be the same as in that simulation, or prescribed but with interactive phenology, or predicted dynamically (Table 2).

Paleogeography and ice sheets were to be kept at their present-day configuration.

175

2.2 Models

The *lig127k* simulations performed with 17 models are evaluated in this paper (Table 2). Of these, 15 used the CMIP6 version of their model that is used for the DECK experiments. The Equilibrium Climate Sensitivity (ECS) varies from 2.1 to 5.3°C.

180

2.3 Calendar adjustments

The output is corrected following Bartlein and Shafer (2019), to account for the impact that the changes in the length of months or seasons over time, related to changes in the eccentricity of Earth's orbit and precession, have on the analysis (i.e. 'celestial' calendar). Not considering the "paleo-calendar effect" can prevent the correct interpretation of
185 data and model comparisons at 127ka, with the largest problems occurring in boreal fall/austral spring (Bartlein and Shafer, 2019).

3 Simulation results

3.1 Preindustrial evaluation

While it is not appropriate to provide a complete evaluation of all the models' pre-industrial simulations here, it is
190 nevertheless important to demonstrate that they are suitable for paleoclimate purposes. Figure 2 presents the climatological temperature (Compo et al., 2011) and precipitation (Adler et al., 2003) determined over the historical, observed period. The ensemble mean difference between each of the model's pre-industrial climatology and these observations is also shown (termed here as ensemble mean bias). The climatological (reanalyzed) surface temperatures are taken from the Early Industrial (1871-1900; Compo et al., 2011) to coincide with the reference
195 frame used for proxy reconstructions. It is clear that the PMIP4-CMIP6 models are in general cooler than the observations, most noticeably in the poles, over land and the NH oceans (Fig. 2). The models are too warm over the



eastern boundary ocean upwelling regions, Atlantic and Indian Ocean sectors of the Southern Ocean, and the Labrador Current - indicating a failure to sufficiently resolve regional ocean circulation features.

200 The climatological zonal mean temperature profile is compared to the simulations (Fig. 3). Whilst the model ensemble compares favorably to the HadCRUT4 database (Morice et al., 2012; Ilyas et al. 2017) in the Tropics, the polar latitudes are still too cold in the simulations (Fig. 3).

205 The piControl simulations of minimum (August-September) Arctic sea ice extent (Figs. 4a and S2), i. e. area where sea ice concentration is at or above 15%, show good agreement with the 15% contour from the HadISST data averaged over the 1870-1920 period (Rayner et al. 2003). Only one of the models, FGOALS-g3, shows greater minimum summer extent in the Nordic Seas as compared to the HadISST period. The simulations of austral summer minimum (February-March) sea ice extent around Antarctica however, show more disagreement among the models and with the HadISST data. One model, LOVECLIM, shows a much greater summer minimum extent, and four models show almost a complete retreat in summer as compared to the HadISST data (Figs. 4b and S4). It should be
210 noted that observations of sea ice coverage during the earliest period available are subject to uncertainty.

215 Due to a lack of sufficiently complete early observations (Adler et al., 2003), a modern climatology of 1971-2000 must be used to compare with the rainfall in the *piControl* simulations. The ensemble bias for both December, January & February (DJF) and June, July & August (JJA) are considered separately given the strongly seasonal nature of precipitation. Models fail to capture the full intensity of rainfall under the Intertropical Convergence Zone (ITCZ), and routinely simulate a South Pacific Convergence Zone (SPCZ) that is too zonal (Brown et al., 2013; Fig. 2). Rainfall associated with the mid-latitude storm tracks is generally too little, and the precipitation over land can show consistent wet and dry biases (Fig. 2).

220 3.2 Surface temperature responses

225 The seasonal character of the insolation anomalies results in strong warming and cooling over the Northern Hemisphere (NH) continents in the *lig127k* ensemble (relative to the *piControl*) in JJA and DJF, respectively. The warming during JJA is greater than 6°C at mid-latitudes in North America and Eurasia (Fig. 5a), though with significant differences among the models (Fig. 5b). Subtropical land areas in the Southern Hemisphere (SH) respond to the positive (but more muted) insolation anomalies, with JJA temperature anomalies more than 2°C. The North Atlantic, North Pacific and Southern Ocean also exhibit warming, with the latter associated with the simulation of winter sea ice around Antarctica, though with large differences across the ensemble of models. Cooling over the Sahel and southern India in JJA is associated with the increased cloud cover associated with the enhanced monsoons (see Section 3.4).

230 The *lig127k* multi-model ensemble simulates cooling during DJF relative to the *piControl*, in response to the negative insolation anomalies at all latitudes (Fig. 5c). The largest DJF temperature anomalies occur over southeastern Asia and northern Africa. Cryosphere (and ocean) memory, particularly lower sea ice area allowing enhanced air-sea



235 interaction, provide the feedback to maintain positive or neutral temperature anomalies annually in the Arctic,
northern Europe, and over the Southern Ocean. As indicated by the standard deviations of the ensemble changes,
large differences in the magnitude of the DJF surface temperature responses, and thus cryosphere feedbacks, exist
across the multi-mean ensemble (Fig. 5d).

240 Annually, the multi-model ensemble changes in surface temperature between the *lig127k* and *piControl* are generally
less than 1°C, except for negative surface temperature anomalies across the North African and Indian monsoon
regions, and positive surface temperature anomalies in the Arctic (Fig. 5e). Large differences exist among the models
in the magnitude of the seasonal and annual surface temperature responses in the polar regions.

245 The large spread of mean annual surface temperature change among the models in the Arctic (60°-90°N) is further
illustrated in Figure 3. The FGOAL-g3 and HadGEM3 simulate 3°C and over 4°C warmer annual surface
temperatures in their *lig127k* simulations than *piControl*, respectively. Two of the models simulate no change or
cooling annually for the Arctic: AWI and ACCESS, respectively. The spread (and magnitude) of mean annual
temperature change for the SH polar region (60-90N) is less, with 7/10 models simulating a modest warming of 0-
1°C, and three models simulating a cooling of the mean annual surface temperature. In the NH monsoon zonal band
250 from 1-30°N, 7/10 models simulate colder mean annual surface temperature, with the other 3 simulating little or no
change.

3.3 Sea ice responses

255 Boreal insolation anomalies at 127 ka enhance the seasonal cycle of Arctic sea ice (Fig. 6), though with notable
differences among the models, varying from relatively small summer reductions in the area extent in the INMCM4-8
and MIROC-ES2L *lig127k* simulations, and much greater reductions in the LOVECLIM and HadGEM3 *lig127k*
simulations. The consensus from the *lig127k* sea ice distributions is a reduced minimum (August-September) summer
sea ice extent (defined as 15% concentration) in the Arctic (Fig. 7) as compared to the *piControl* simulations. Sea ice
remains above 15% concentrations over the central Arctic Ocean in all but one of the *lig127k* simulations (Fig.7, Fig.
260 S3). One model (HadGEM3) has the Arctic becoming ice-free during August-September.

From January through April, all but two of the models simulate a boreal winter Arctic areal extent similar in their
lig127k and *piControl* simulations. HADGEM3 and EC-Earth showing small reductions of Arctic sea ice extent in
boreal winter and spring.

265 The minimum (February-March) austral summer sea ice around Antarctica is similar in the *lig127k* and *piControl*
simulations (Fig. 7), though with widely different distributions among the models (Fig. S5). Those models that
simulate summer sea ice in the Weddell Sea in the *piControl*, (Fig. S4) retain this sea ice in their *lig127k* simulation.
The maximum austral winter sea ice around Antarctica varies widely among the models, with the MIROC-ES2L



270 simulating the lowest areal extent (and seasonal cycle) and LOVECLIM and IPSLCM6 simulating the highest areal extent (and seasonal cycle) (Fig. 6) in the *piControl* and *lig127k* simulations.

It is interesting to compare the simulated summer sea ice extents in the *lig127k* simulations to the observed sea ice extents for 2000-2018 (black lines in Fig. 7). More than half of the models simulate a retreat of the Arctic minimum (August-September) ice edge at 127ka, similar to the average of the last 2 decades. The pattern of February-March Southern Ocean sea ice extent is broadly similar in the *lig127k* simulations to 2000-2018, though 4 models simulate a larger sea ice area.

280 There appears to be a relationship between the Equilibrium Climate Sensitivity (ECS) (Table 2) and simulation of August-September *lig127k* minimum Arctic sea ice area (Fig. 8). CESM2 with an ECS of 5.3°C simulates a small August-September *lig127k* Arctic sea ice area, while INM-CM4-8 with an ECS of 2.1°C simulates the largest August-September *lig127k* Arctic sea ice area.

285 Interestingly, the *lig127k* minimum Arctic sea ice area anomalies show a strong negative correlation (-0.83) with the Arctic (60-90°N) annual surface temperature anomalies for the respective *piControl* simulations but only a weak correlation (-0.40) with the corresponding JJA temperature anomalies (Fig. 8). for the respective *piControl* simulations. Memory in the ocean and cryosphere memory provide feedbacks to maintain larger positive temperature anomalies, DJF and annually, in the Arctic than in JJA (Figs. 5 and 11).

290 Previous studies suggest that the mean-ice state in the control climate can influence the magnitude and spatial distribution of warming at high-latitudes in future projections (Holland and Bitz, 2003). Thinner Arctic sea ice is more susceptible to summer melting than thicker Arctic sea ice. Figure 8 investigates if this relationship holds for the models in the multi-model ensemble. Arctic sea ice thickness, averaged for model grid cells with at least 15% concentration, varies substantially across the 1850 CE ensemble, ranging from 1-1.5m in CMRM-CM6-1 and 295 NESM3 to ~7.5m in MIROC-ES2L. No robust relationship to the August-September *lig127k* minimum Arctic sea ice area anomaly is present. One reason for a lack of any relationship may be the seasonal nature of the *lig127k* insolation forcing as compared to the annual forcing by greenhouse gas changes in future projections.

3.4 Precipitation responses

300 The seasonal character of the insolation anomalies results in enhanced summer monsoonal precipitation in the *lig127k* ensemble (relative to the *piControl* ensemble) over northern Africa, extending into Saudi Arabia, India and southeast Asia, and northwestern Mexico/southwestern U.S (Figs. 9, 10). In contrast, summer monsoonal precipitation decreases occur over South America, southern Africa, and Australia. The spread among models is large, however, as shown by the standard deviations of ensemble changes of the precipitation changes (Fig. 9 and percentage changes in area-averaged precipitation during the monsoon season for seven different regional monsoon 305 domains for the individual *lig127k* simulations (Fig. 16). The models generally agree on the sign of the percentage changes in the area-averaged precipitation rate during the monsoon season for the monsoon regions, except for the



South Asian and Australian-Maritime Continent monsoons where some models are simulating increased monsoonal precipitation whereas others are showing decreases.

310 Over the tropical Pacific Ocean, reduced DJF precipitation over the ITCZ is a robust feature across the ensemble of *lig127k* simulations. The models simulate a shift of the tropical Pacific ITCZ northward in JJA and southward in DJF, though with significant differences among the models of the ensemble. Over the Indian Ocean, the ensemble mean indicates more precipitation in DJF over the entire basin and less in JJA, particularly in the central and eastern basin, though with large standard deviations.

315

Figure 10 shows the ensemble-averaged *lig127k* change in monsoon-related rainfall rate and global monsoon domain. Increases in the summer rainfall rate and areal extent of the North Africa and East Asia monsoon are clear, and are robust across the multi-model ensemble. The spread across the multi-model ensemble is considerable, though, for the North African (NAF) monsoon, with the percentage change in the areal extent varying from ~40-
320 120% (Fig. 18b) and the percentage change in the total amount of water precipitated in each monsoon season varying from ~70-140% (Fig. 18c). The models are in closer agreement for the East Asian monsoon (EAS), with the percentage change in the areal extent varying from ~10-35% (Fig. 18b) and the percentage change in the total amount of water precipitated in each monsoon season varying from ~25-40% (Fig. 18c). The *lig127k* and *piControl* simulations produce more muted changes for the other monsoon regions in the multi-model ensemble, with regards
325 to the regional monsoon-related rainfall rate and the monsoon domains (Fig. 10).

4 Data reconstructions

4.1 Marine temperatures

The *lig127k* climate model simulations are assessed using two complementary compilations of sea surface temperature (SST) anomalies at 127 ka (Tables S1 and S2), which are both individually based on stratigraphically
330 consistent chronologies (Capron et al., 2017; Hoffman et al., 2017).

The multi-archive high-latitude compilation by Capron et al. (2014, 2017) includes 42 sea surface annual/summer temperature records with a minimum temporal resolution of 2 kyr for latitudes above 40°N and 40°S, along with 5 ice core surface air temperature records. In contrast, the global marine compilation by Hoffman et al. (2017) includes 186 annual, summer and winter SST records from the Atlantic, Indian and Pacific oceans, with a minimum temporal
335 resolution of 4 kyr on their published age models. Note that, in addition to the annual microfossil assemblage SST records calculated for 41 sites as the average of the summer and winter records with a model- and observation-consistent correction for annual offsets (Hoffman et al., 2017), we also provide here for these specific sites the updated seasonal (summer and winter) SST estimates on the Hoffman et al. age models. SST from marine cores are reconstructed in both compilations from foraminiferal Mg/Ca ratios, alkenone unsaturation ratios or microfossil
340 faunal assemblage transfer functions (Capron et al., 2014, 2017; Hoffman et al., 2017).



To derive the LIG marine chronologies, both compilations make use of the climate model-supported hypothesis that surface-water temperature changes in the sub-Antarctic zone of the Southern Ocean (respectively in the North Atlantic) occurred simultaneously with air temperature variations above Antarctica (respectively Greenland) (Capron et al., 2014; Hoffman et al., 2017). The compilation by Hoffman et al. (2017) then uses basin-synchronous LIG
345 changes in the oxygen isotopic composition of benthic foraminifera, as observed in previous studies of benthic foraminiferal isotope changes across glacial terminations (Lisiecki and Raymo, 2009) within the same ocean basins, to align intra-basin chronologies. However, a major difference is the underlying reference chronology used in both compilations: the Antarctic Ice Core Chronology 2012 (AICC2012) (Bazin et al., 2013; Veres et al., 2013) in the compilation by Capron et al. (2014, 2017), and a chronology based on millennial-scale variations
350 observed in independently-dated Asian speleothem records (Speleo-Age) (Barker et al., 2011) in the compilation by Hoffman et al. (2017). Note that the two reference chronologies diverge by about 1 ka at 127 ka (Capron et al., 2017).

The two compilations then follow quite similar Monte Carlo approaches to propagate temperature and chronological uncertainties. Indeed, both compilations generate 1000 realizations of the site-specific surface temperature records to
355 integrate the uncertainty on the temperature reconstruction's method, and both produce 1000 possible chronologies to propagate the relative age uncertainty related to alignment of records. For a given site, the temperature at 127 ka is the temperature value directly taken at 127 ka in the compilation by Hoffman et al. (2017), using dated temperature timeseries interpolated every 1 ka. In the compilation of (Capron et al., 2014, 2017), the temperature at 127 ka is taken as the median temperature averaged over the 128-126 ka period. Finally, temperatures anomalies relative to
360 preindustrial are calculated in both cases for marine sites using the HadISST dataset (Rayner et al., 2003), over the intervals 1870-1899 CE and 1870-1889 CE, in the compilations by Capron et al. (2017) and Hoffman et al. (2017), respectively. For both compilations, the provided 2-sigma uncertainties integrate errors linked to relative dating and surface temperature reconstruction methods.

Nevertheless, because of: (1) the different reference chronologies used, (2) the different tie-points and associated
365 relative age uncertainties defined to derive the chronology of each site, and (3) the different calculation methods (Bayesian statistics versus linear interpolation between tie-points) used in the Monte Carlo age model analysis of each site (despite apparently relatively similar approaches), the two compilations by Capron et al. (2014, 2017) and by Hoffman et al. (2017) cannot be merged and have been considered separately. Implications of these
370 methodological differences on the inferred 127 ka values are best illustrated when comparing the surface temperature timeseries deduced from the two different approaches for a same North Atlantic (62°N) site: at 127 ka, a temperature offset of ~2°C is observed between the two reconstructions (see Figure 4 of Capron et al., 2017).

4.2 Ice core temperatures

Surface air temperature records for one site (NEEM) on the Greenland ice sheet and four sites on the Antarctic ice
sheet are deduced from ice core water isotopic profiles (Capron et al., 2014, 2017) (Table S3). For ice cores,
375 preindustrial conditions are estimated using borehole temperature measurements for Greenland, and 1870-1899 CE



water isotopic profiles for Antarctic (Capron et al., 2017). Temperatures are again the median for the 126-128 ka period, and are considered to represent annual averages. Uncertainty is estimated using the same Monte Carlo procedure as was used for the marine cores in the compilation of Capron et al. (2017). Because it uses the same reference timescale (AICC2012) the ice core dataset can be considered coherent with the marine SST dataset of Capron et al (2017).

380

4.3 Terrestrial temperatures

Calibrated, well-dated reconstructions of Last Interglacial temperatures over the continents are quite limited. We have assembled two distinct compilations of continental air temperature reconstructions: a dataset of air temperatures over Europe at 127 ka based on Brewer et al., 2008, and a compilation of peak Last Interglacial summer temperatures reconstructed at Arctic sites from pollen and insect assemblages (Table S4). For both we report anomalies comparing reconstructed temperatures with preindustrial climate estimated from 1871-1900.

385

In Europe, favorable geological conditions have led to the accumulation of numerous LIG sediment sequences from a variety of depositional environments (Tzedakis, 2007). These include former kettle lakes overlying late Saalian (MIS 6) till, depressions left by the penultimate alpine glaciation or local ice caps, and volcanic crater lakes or tectonic grabens mainly in the unglaciated south. Over several decades, a substantial body of pollen evidence has provided an insight into the LIG vegetational development across Europe. A number of pollen-based climate reconstructions on reference sequences have been attempted, using a variety of methods. However, differences between underlying assumptions and data employed (e.g. taxon presence-absence *versus* abundance) mean that results have been difficult to compare.

390

395

Here, we include data from one study that has applied a multi-method approach to assess combined uncertainties of reconstruction and age models on a set of reference pollen records (Brewer et al., 2008). The reconstruction methods used are (i) partial least squares, (ii) weighted average partial least squares, (iii) generalized additive models, (iv) artificial neural network, (v) unweighted modern analogue technique, (vi) weighted modern analogue technique, and (vii) revised analogue method using response surfaces. Timescales for the pollen sequences were developed by transferring the marine chronology to land sequences for certain pollen stratigraphical events on the basis of joint pollen and palaeoceanographic analyses in deep-sea sequences on the Portuguese Margin and Bay of Biscay (Shackleton et al., 2003; Sánchez Goñi et al., 2008). With particular reference to constraining the 127 ka timeslice, the pollen stratigraphical events used were the onset of the *Quercus* (128.8 ± 1 ka) and *Carpinus* (124.77 ± 1 ka) expansions (Brewer et al., 2008). For each site, chronological uncertainties were estimated at each sample by randomly sampling an age from the range around each control point, fitting a linearly interpolated age model and repeating this 1000 times (Brewer et al., 2008). Reconstructions were made at 500 yr intervals by randomly sampling within the chronological uncertainties and reconstruction errors for each method, resulting in 1400 estimates for each time t (Brewer et al., 2008). Here we present the mean value and standard deviation for mean annual temperature, mean temperature of the coldest month and mean temperature of the warmest month across all sites for 127 ka. Of

400

405

410



the seventeen sites used by Brewer et al. (2008), four were excluded because they either did not extend to 127 ka or were from marine pollen records.

415 The Arctic dataset compiles the most stratigraphically complete, well-constrained calibrated summer temperature
reconstructions published from each subregion of the Arctic above 65°N latitude. We report the mean of the two
warmest consecutive reconstructions at each site, utilizing the original published models and reconstructions. For
sites where both insect- and pollen-based temperature reconstructions have been published, or where multiple models
have been applied to the same proxy, we report here the average of those reconstructions. We report the original
published model uncertainties (e.g., root mean square error of prediction for weighted averaging models), including
420 the most conservative (largest) model uncertainties for sites where multiple proxies/models are applied. Importantly,
the Arctic compilation differs from all other paleotemperature datasets used here, in that it reports the warmest LIG
conditions registered at each site rather than temperatures at 127 ka. This approach was necessitated by the coarse
temporal resolutions and chronologies of the North American Arctic reconstructions, which come from
stratigraphically discontinuous deposits dated by ¹⁴C (non-finite ¹⁴C ages) and in some cases luminescence or
425 tephrochronology. In contrast to the North American Arctic sites, in northern Finland (Sokli) and northeast Russia
(El'gygytgyn) correlative dating provides continuous chronologies. The reported peak warmth at those sites occurred
at ~125 and 127-125 ka, respectively (Melles et al. Science 2012; Salonen et al. Nature Comms 2018). Reconstructed
temperature at Sokli at 127 ka was ~1°C lower than the peak temperature reported here from that site. The Greenland
ice core-derived temperature reconstruction from NEEM complements the Arctic terrestrial dataset, but it reflects
430 annual rather than summer-specific climate.

4.4 Arctic sea ice

A summary of LIG sea ice data obtained from marine cores in the Arctic, Nordic Seas and northern North
Atlantic, their interpretation, and comparison to the *lig127k* simulations can be found in Kageyama et al. (2019). The
sea ice records are derived from dinoflagellate cysts, subpolar foraminers, and ostracods.

435 4.5 Precipitation

Compilation of the existing proxy evidence for LIG precipitation have been presented for the Northern Asian and
circum-Arctic region (CAPE, 2006; Kim et al., 2010; Velichko et al., 2008). Recently, a compilation with near-global
coverage was presented in Scussolini et al. (2019), including 138 proxy sites based on different types of proxies and
archives, mostly from pollen, lacustrine sediment composition, speleothem, and multi-proxy reconstructions. This, in
440 contrast to previous work, aimed to select proxy signals approximately corresponding to 127 ka, in order to facilitate
comparison with results from the *lig127k* simulations of PMIP4. The main patterns that emerge, about precipitation
change between the LIG and the pre-industrial/recent past, are near-ubiquitous higher LIG annual precipitation over
the NH (Fig. 14). Exception to this are individual sites in western North Africa, the Levant, northern South America,
Borneo, the northwest of modern United States and Alaska, northern Scandinavia, and northern Siberia. Over the SH,
445 the proxy signal is more irregular: Australia and the west coast of South America have proxies predominantly



indicating higher precipitation in the LIG, sites in the rest of South America indicate lower precipitation or no change and over southern Africa changes are geographically more heterogeneous.

5 Model-data comparisons

5.1 Temperature

450 NH high-latitude terrestrial temperature proxies for the boreal summer (JJA) match the large warming from the
lig127k ensemble for the Canadian, Greenland and Scandinavian sites (Figure 11). On the other hand, although the
models also simulate large warming over Alaska and Siberia in JJA, these sites have temperature anomalies near
zero. Over Europe the temperature proxies can indicate substantial warmings right next to substantial coolings
making a credible comparison difficult, though a much weaker lapse rate at 127 ka (Brewer et al., 2008) might be
455 responsible for the differences. Over the North Atlantic, the model and proxy JJA temperature anomalies are
generally in good agreement. The exceptions are in the northwestern North Atlantic and the Nordic Sea, where the
Capron data suggest significant cooling. This mismatch could be associated with meltwater from potentially remnant
ice sheets over Canada and Scandinavia, which ice sheets the *lig127k* simulations do not incorporate. The multi-
model ensemble indicates austral winter (JJA) warming over the Southern Ocean and Antarctica, but the lack of
460 proxies does not allow an assessment.

The marine reconstruction of Capron et al (2017) provides evidence of significant LIG warm temperature anomalies
for the austral summer (DJF) over the Southern Ocean, which is not exhibited by the ensemble mean. In the NH, the
multi-model ensemble indicates much warmer surface temperatures in DJF over the Arctic Ocean, Baffin Bay, and
465 Labrador and Greenland Seas, which cannot be evaluate given the available reconstructions. Simulated LIG DJF
temperatures over North America and Eurasia are significantly colder with respect to preindustrial, except over
western Europe. The proxies for the latter again show a mixed signal.

The most consistent picture from the temperature proxies representing annual conditions is warmer LIG temperatures
470 over Greenland and Antarctica. The ensemble mean matches the pattern but not the magnitude of LIG temperature
anomalies over the polar ice sheets reconstructed from the ice cores. However, the model spread in the temperature
response averaged over the 60-90°latitude range is large as shown in Fig. 2, and thus, some models may compare
more favorably with the temperature proxies than others, which pulls down the mean response. It should also be
noted that internal variability is large in high latitudes, which can also hinder data-model comparisons. Elsewhere, at
475 high latitudes in both hemispheres, the temperature proxy reconstructions indicate a mixed response at LIG.

At low latitudes (40°S – 40°N), marine proxy data from the Hoffman reconstruction are available (Fig. 12). They
generally correspond with the ensemble mean changes. The SST proxies from the tropical Atlantic match the colder
lig127k SSTs in DJF. But the reconstructed cooling there in JJA is not captured by the simulations, leading to a
480 failure to capture the annual mean signal. Proxy indications of much warmer SSTs in the upwelling regions off the
west coasts of South Africa, North America, and South America are not simulated by the models. The resolution of



CMIP models is generally not adequate to properly simulate these narrow coastal upwelling regions, and their warm bias in the preindustrial simulations (Fig. 2) leaves little potential for strong SST increases.

485 5.2 Precipitation

As shown in a comparison with a similar ensemble (Scussolini et al., 2019), precipitation proxies from the global compilation largely match the higher precipitation from the models included in the *lig127k* ensemble over much of the NH continents: over most of northern Africa, the Middle-East, the Mediterranean, South and East Asia, northeast
490 Asia, and North America (Fig 10). Proxies and models weakly disagree over much of Europe, Central Asia and the region between them, where proxies indicate wetter LIG conditions or no change, and the ensemble average indicates somewhat drier conditions or no change. Other instances of disagreement in the NH are over the southern side of Northern Africa, with drier proxies and wetter models, and over the Mississippi basin, with a wetter proxy site and somewhat drier model average. However, the coastal proxy sites near the Bay of Bengal, which show strongly drier
495 conditions, are near the region of strongly drier conditions over the Atlantic suggesting a northward shift in the ITCZ. In the SH, proxies and models mostly agree over South America, while they disagree over Australia and in several locations over southern Africa, where many proxies and models indicate wetter and drier LIG, respectively. More details of a comparison with a similar model ensemble can be found in Scussolini et al. (2019).

6 Comparison of the model sensitivities to the insolation anomalies at 127 ka and 6 ka

500 The large-scale features and evaluation of the CMIP6/PMIP4 *midHolocene* simulations in comparison to data reconstructions and in the CMIP5/PMIP3 endeavor can be found in Brierley et al., 2020). In this section, we briefly explore differences in the responses of surface temperature, monsoon precipitation, and Arctic sea to the different magnitudes and seasonal character of the insolation anomalies at 127 ka versus 6 ka.

6.1 Orbital forcing

505 The orbit at 6 ka was characterized by a smaller eccentricity than at 127 ka, similar to 1850 CE. Perihelion occurred near the boreal autumn equinox as compared to close to the boreal summer solstice at 127ka and near aphelion at 1850CE. NH summer insolation anomalies at 6ka, ~5-10% greater than at 1850 CE, are considerably less than at 127ka (Fig. 1 and Fig. 14). In addition, the positive insolation anomalies of greater than 10% in the Arctic occur in July-August at 6ka as compared to May-August at 127 ka. At SH mid- and high latitudes, the anomalous insolation
510 anomalies are shifted to boreal fall/austral spring. As such, the orbital forcing on climate is expected to be stronger at 127 ka than at 6 ka.

6.2 Surface temperature responses

Figure 15 compares the multi-model ensemble average changes and standard deviations of ensemble changes of surface air temperatures (°C) for *lig127k* and *midHolocene* simulations. In the tropics and Southern Hemisphere, the JJA zonal
515 average temperature anomaly is positive (~ +0.5°C) for the *lig127k* ensemble but negative (~ -0.5°C) in the *midHolocene* ensemble. The maximum JJA surface temperature anomalies occur at ~40°-65°N for both time periods



but are significantly greater at 127ka (over 3°C at 127 ka as compared to ~1°C at 6 ka). The DJF zonal-average surface temperature anomalies are near zero or slightly negative south of 65°N for both time periods. Cryosphere and ocean feedbacks provide the memory for positive surface temperature anomalies in DJF, even with negative insolation anomalies, with DJF Arctic surface temperatures averaging about 0.5°C higher in the *midHolocene* ensemble mean and up to 3°C higher in the *lig127k* ensemble mean than the *piControl*.

6.3 Precipitation responses

The sign of the percentage change in the areal extents of the regional monsoon domain (Aav) and the percentage change in the total amount of water precipitated in each monsoon season (Totwater) are similar for the *lig127k* and *midHolocene* simulations as compared to *piControl* simulations, but the responses are generally enhanced in the *lig127k* simulations as compared to the *midHolocene* simulations (Fig. 16). Both time periods show greater areal extent and total amount of water precipitated for the NAF and EAS monsoons. Notable is that all but two of the models have greater areal extent and all but one of the models show greater increases in total water precipitated for the NAF monsoon in the *lig127k* simulations as compared to the changes in the *midHolocene* simulations. Similarly, the Australian-maritime Continent, South Africa, and South America monsoons show greater reductions of areal extent and total water precipitated in the *lig127k* simulations than in the *midHolocene* simulations as compared to the *piControl* simulations. Both time periods show a mixed simulated response of the North American monsoons. The mid-continental Eurasian rainfall noted by Bartlein et al, (2017) in the mid-Holocene appears to also occur at 127 ka, where simulations indicate a weak drying or no change while proxies suggest it was wetter (Fig. 13).

6.4 Arctic sea ice responses

The boreal insolation anomalies at 6 ka enhance the seasonal cycle of Arctic sea ice, though much less so than in the *lig127k* simulations (Fig. 17). None of the models currently in this analysis have the Arctic becoming ice-free in their *midHolocene* simulations.

7 Conclusions

The Tier 1 *lig127k* experiment was designed to address the climate responses to stronger orbital forcing (relative to the *midHolocene* experiment) using the same state-of-the-art models and following a common experimental protocol. At 127 ka, atmospheric greenhouse gas levels were similar to those of the preindustrial period, land ice likely only remained over Greenland, and Antarctica, and the continental configurations were almost identical to modern. In addition, within uncertainties in chronology and dating, this time period allows data reconstructions for comparison to the model simulations allowing an assessment of responses to the large insolation changes, yet does not include the effects of the Heinrich 11 meltwater event. The 17 models that have completed the *lig127k* experiment are presented.

The CMIP6-PMIP4 *lig127k* simulations show strong warming and cooling over the NH continents during JJA and DJF, respectively, in response to the seasonal character of the insolation anomalies. The JJA ensemble average warming is greater than 6°C at mid-latitudes in North America and Eurasia, though with significant differences



among the models. The simulations exhibit reduced minimum (August-September) summer sea ice extent (defined as 15% concentration or greater) in the Arctic, but with substantial differences among the ensemble and one model having the Arctic becoming ice-free in late summer. Cryosphere and ocean memory and increased air-sea interaction provide the feedback to maintain positive temperature anomalies in the *lig127k* simulations annually in the Arctic, northern Europe, and over the Southern Ocean, though again with a large spread across the model ensemble. As expected from the larger insolation anomalies in the *lig127k* than *midHolocene* simulations, the boreal summer responses in NH surface temperature and Arctic sea ice are amplified.

The CMIP6-PMIP4 *lig127k* simulations produce enhanced summer monsoonal precipitation and areal extent over northern Africa, which extends into Saudi Arabia, India and southeast Asia, and northwestern Mexico/southwestern U.S. In contrast, summer monsoonal precipitation decreases over South America, southern Africa, and Australia. The spread across the multi-model ensemble is particularly large for the North African monsoon, for the percentage change in its areal extent and total amount of water precipitated during the monsoon season. The *lig127k* individual monsoon changes are of a similar sign, but a greater magnitude, to those seen in the *midHolocene* simulations (Brierley et al., 2019).

New syntheses for surface temperature and precipitation, targeted for 127ka, have been developed for comparison to the CMIP6-PMIP4 *lig127k* simulations. The surface temperature reconstructions include two complimentary compilations of SST based on stratigraphically consistent chronologies, surface air temperatures from the Greenland and Antarctic ice sheets deduced from the ice core water isotopic profiles, continental air temperatures for Europe based on pollen records, and peak LIG summer temperatures in the Arctic. Anomalies were consistently computed comparing the reconstructed temperatures with preindustrial climate estimate from the end of the 19th century. A new precipitation reconstruction has expanded from previous regional compilations to now near-global coverage.

Over Canada, Scandinavia, and the North Atlantic, the proxy and *lig127k* positive JJA temperature anomalies are in good agreement. The exceptions are in the northwestern North Atlantic and the Nordic Sea, where the Capron reconstruction suggest significant cooling. Capron reconstruction also provides evidence of significant positive DJF temperature anomalies over the Southern Ocean, which is not exhibited by the ensemble mean. These mismatches could be associated with meltwater from potentially remnant ice sheets over Canada and Scandinavia as well as memory in the ocean of the H11 event (Marino et al., 2015), which the *lig127k* simulations do not incorporate, leading to cooling in the North Atlantic and warming in the Southern Ocean (Stone et al., 2016).

The most consistent picture from the temperature proxies representing annual conditions is warmer LIG temperatures over Greenland and Antarctica. The ensemble mean matches the pattern but not the magnitude of LIG temperature anomalies over the polar ice sheets reconstructed from the ice cores. However, the model spread is large. The *lig127k* Tier 1 experiment protocol prescribed modern Greenland and Antarctic ice sheets rather than allowing them to evolve to smaller and lower ice sheets of the *lig127k* climate. A modeling study with the HadCM3 (a CMIP3 model)



590 demonstrated that the distinctive peak in $\delta^{18}\text{O}$ observed in Antarctic ice cores at 128 ka was likely due to the loss of winter sea ice in the Atlantic, Indian, and Pacific sectors of the Southern Ocean. To achieve this winter sea ice extent required forcing by the H11 meltwater event (Holloway et al., 2017, 2018). The CMIP6-PMIP4 Tier 2 LIG experiments (*lig127k-H11*, *lig127-gris*, *lig127k-ais*) will allow modeling groups to explore the effects of the H11 meltwater event and the Antarctic and Greenland ice sheets at their minimum LIG extent and lower elevations (Otto-Bliesner et al., 2016).

595 Other reasons for mismatches between the models and the reconstructions for temperature and precipitation will also be explored with CMIP6-PMIP4 Tier 2 LIG experiments. Most of the models contributing to the *lig127k* still do not include interactive vegetation. An intercomparison of the responses of the *lig127k* simulations with interactive vegetation would be useful. The CMIP6-PMIP4 Tier 2 *lig127k-veg* experiments will consider the sensitivity of the responses to prescribed boreal forests in the Arctic and shrub/savanna over the Sahara, separately and together.

600 Incorporating these vegetation changes has been shown to impact the albedo and evapotranspiration on the surface energy and water budgets, reducing model and data mismatches at high latitudes (Swann et al., 2010) and for the North African monsoon (Pausata et al., 2016). Additionally, the CMIP6 models do not currently simulate changes to soil texture or color for different climate states. A previous modeling study suggests that soil feedback can drive the African monsoon northward during interglacials (Levis et al., 2004).

605 Despite an abundance of LIG pollen records from Eurasia and various attempts at pollen-based climate reconstructions (e.g. compilations Velichko et al., 2007; Turney & Jones 2010), chronological and methodological uncertainties continue to complicate comparisons with climate model outputs. The lack of spatial coherence in the European temperature reconstructions may reflect depth-age model issues at individual sites, which implies that the 610 127 ka timeslice had not been correctly identified. An alternative approach would have been to select peak temperatures from a wider interval (e.g. 127 ± 2 ka) and assume that these are quasi-synchronous. However, closer inspection of the Brewer et al. (2008) data reveals that the timing of peaks in annual and JJA temperatures are often not synchronous. In addition, the Arctic reconstruction may be skewed a bit warmer than the models, given that by definition this reconstruction is reporting the warmest period from each Arctic site, rather than the 127 ka timeslice.

615 Temperature reconstructions are not available for many regions where the *lig127k* multi-model ensemble show interesting responses to the *lig127k* forcing. These include the polar regions during their respective winter seasons: Arctic and North Atlantic Oceans in DJF and Southern Ocean and Antarctica in JJA. Development of terrestrial reconstructions for most continents and marine reconstructions for the Indian and Pacific Oceans would be useful for 620 assessing the model responses.

The CMIP6-PMIP4 *lig127k* experiment has potential implications for confidence in future projections. Large differences exist among the models in the magnitude of the seasonal and annual surface temperature responses in the polar regions reflecting differences in the feedbacks processes represented by each model. These should be



625 investigated. More than half of the models simulate a retreat of the Arctic minimum (August-September) ice edge at
similar to the average of the last 2 decades. The models contributing to the *lig127k* ensemble have an Equilibrium
Climate Sensitivity (ECS) varying from 2.1 to 5.3°C. There appears to be a clear relationship between the ECS of
each model and its simulation of August-September *lig127k* minimum Arctic sea ice extent. With very limited Arctic
sea ice proxies for 127 ka, and with evolving interpretation of the relationships of these proxies with sea ice coverage
630 (Stein et al., 2017; Kageyama et al., 2020), it is difficult to rule out the high or low values of ECS from the proxy
data. Warmer summer temperatures over Greenland, warmer oceans year-round surrounding Greenland, and reduced
Arctic summer sea ice all have the potential to force a retreat of the ice sheet in the future. The *lig127k* results can be
used to force Greenland ice sheet models, both one-way as included in the ISMIP6 protocols (Nowicki et al., 2016)
and fully coupled to a climate model as is now being done by several modeling groups. With the availability of LIG
635 ice and marine core records, LIG simulations with an evolving Greenland ice sheet will allow an assessment of the
corresponding future projection simulations.

640

Data availability. The model results for the *lig127k* and *piControl* simulations are archived on the CMIP6 ESGF websites. The data are included as tables in the Supplementary Material.

645

Author contributions. BLO-B, AZ, ECB and CB performed the bulk of the writing and analysis. YA–AW contributed data, text and analysis to the research. AA–O–WZ contributed the modeling simulations for the manuscript.

650

Competing interests. The authors declare no competing interests.

655

Acknowledgements. BLO-B, ECB and RT acknowledge the CESM project, which is supported primarily by the National Science Foundation (NSF). This material is based upon work supported by the National Center for Atmospheric Research (NCAR), which is a major facility sponsored by the NSF under Cooperative Agreement No. 1852977. Computing and data storage resources, including the Cheyenne supercomputer (doi:10.5065/D6RX99HX), were provided by the Computational and Information Systems Laboratory (CISL) at NCAR. CJRW acknowledges the financial support of the UK Natural Environment Research Council-funded SWEET project (Super-Warm Early Eocene Temperatures), research grant NE/P01903X/1 and the financial support of the Belmont-funded PACMEDY (PALaeo-Constraints on Monsoon Evolution and Dynamics) project. LM acknowledges support from the Australian Research Council FT180100606.

660

This work is a contribution to the PAGES QUIGS Working Group and the PMIP project. We acknowledge the World Climate Research Programme's Working Group on Coupled Modelling, which is responsible for CMIP, and we thank the climate modeling groups for producing and making available their model output.

665



References

- 670 Adler, R. F., Huffman, G. J., Chang, A., Ferraro, R., Xie, P.-P., Janowiak, J., Rudolf, B., Schneider, U., Curtis, S.,
Bolvin, D., et al.: The version-2 global precipitation climatology project (GPCP) monthly precipitation analysis
(1979–present), *Journal of hydrometeorology*, 4, 1147–1167, 2003.
- Albani, S., Mahowald, N. M., Winckler, G., Anderson, R. F., Bradtmiller, L. I., Delmonte, B., François, R., Goman,
M., Heavens, N. G., Hesse, P. P., Hovan, S. A., Kang, S. G., Kohfeld, K. E., Lu, H., Maggi, V., Mason, J. A.,
675 Mayewski, P. A., McGee, D., Miao, X., Otto-Bliesner, B. L., Perry, A. T., Pourmand, A., Roberts, H. M.,
Rosenbloom, N., Stevens, T., and Sun, J.: Twelve thousand years of dust: the Holocene global dust cycle
constrained by natural archives, *Clim. Past*, 11, 869–903, <https://doi.org/10.5194/cp-11-869-2015>, 2015.
- Bakker, P., Stone, E. J., Charbit, S., Gröger, M., Krebs-Kanzow, U., Ritz, S. P., Varma, V., Khon, V., Lunt, D. J.,
Mikolajewicz, U., Prange, M., Renssen, H., Schneider, B., and Schulz, M.: Last interglacial temperature evolution
– a model inter-comparison, *Clim. Past*, 9, 605–619, <https://doi.org/10.5194/cp-9-605-2013>, 2013.
- 680 Barker, S., Knorr, G., Edwards, R. L., Parrenin, F., Putnam, A. E., Skinner, L. C., Wolff, E. and Ziegler, M.: 800,000
Years of Abrupt Climate Variability, *Science*, 334(6054), 347–351, doi:10.1126/science.1203580, 2011.
- Bartlein, P. J., Harrison, S. P., and Izumi, K.: Underlying causes of Eurasian midcontinental aridity in simulations of
mid-Holocene climate, *Geophysical research letters*, 44, 9020–9028, 2017.
- Bartlein, P. J. and Shafer, S. L.: Paleo calendar-effect adjustments in time-slice and transient climate-model
685 simulations (PaleoCalAdjust v1. 0): impact and strategies for data analysis, *Geoscientific Model Development*,
12, 3889–3913, 2019.
- Bazin, L., Landais, A., Lemieux-Dudon, B., Toyé Mahamadou Kele, H., Veres, D., Parrenin, F., Martinerie, P., Ritz,
C., Capron, E., Lipenkov, V., Loutre, M. F., Raynaud, D., Vinther, B., Svensson, A., Rasmussen, S. O., Severi,
M., Blunier, T., Leuenberger, M., Fischer, H., Masson-Delmotte, V., Chappellaz, J. and Wolff, E.: An optimized
690 multi-proxy, multi-site Antarctic ice and gas orbital chronology (AICC2012): 120-800 ka, *Clim Past*, 9(4), 1715–
1731, doi:10.5194/cp-9-1715-2013, 2013.
- Berger, A. and Loutre, M. F.: insolation values for the climate of the last 10 000 000 years, *Quaternary Sci. Rev.*, 10,
297–317, [https://doi.org/10.1016/0277-3791\(91\)90033-q](https://doi.org/10.1016/0277-3791(91)90033-q), 1991.
- Braconnot, P., Harrison, S. P., Kageyama, M., Bartlein, P. J., Masson-Delmotte, V., Abe-Ouchi, A., Otto-Bliesner,
695 B., and Zhao, Y.: Evaluation of climate models using palaeoclimatic data, *Nature Climate Change*, 2, 417–424,
2012.
- Braconnot, P., S. Joussaume, N. de Noblet, and G. Ramstein, Mid-Holocene and last glacial maximum African
monsoon changes as simulated within the Paleoclimate Modeling Intercomparison project, *Global and Planetary
Change*, 26, 51-66, 2000.
- 700 Brewer, S., Guiot, J., Sánchez Goñi, M.F. & Klotz, S.: The climate in Europe during the Eemian: a multi-method
approach using pollen dat., *Quat. Sci. Rev.*, 27, 2303-2315, 2008.
- Brown, J. R., Moise, A. F., and Colman, R. A.: The South Pacific Convergence Zone in CMIP5 simulations of
historical and future climate, *Climate dynamics*, 41, 2179–2197, 2013.
- Brierley, C. M., A. Zhao, S. P. Harrison, P. Braconnot, C. J. R. Williams, D. J. R. Thornalley, X. Shi, J.-Y.
705 Peterschmitt, R. Ohgaito, D. S. Kaufman, M. Kageyama, J. C. Hargreaves, M. P. Erb, J. Emile-Geay, R.
D’Agostino, D. Chandan, M. Carré, P. Bartlein, W. Zheng, Z. Zhang, Q. Zhang, H. Yang, E. M. Volodin, C.
Routson, W. R. Peltier, B. Otto-Bliesner, P. A. Morozova, N. P. McKay, G. Lohmann, A. N. Legrande, C. Guo, J.
Cao, E. Brady, J. D. Annan, and A. Abe-Ouchi: Large-scale features and evaluation of the PMIP4-CMIP6
midHolocene simulations, submitted to *Clim. Past*, 2020.
- 710 CAPE-Last Interglacial Project Members: Last Interglacial Arctic warmth confirms polar amplification of climate
change, *Quat. Sci. Rev.* 25, 1383–1400, 2006.
- Capron, E., Govin, A., Stone, E. J., Masson-Delmotte, V., Mulitza, S., Otto-Bliesner, B., Rasmussen, T. L., Sime, L.
C., Waelbroeck, C. and Wolff, E. W.: Temporal and spatial structure of multi-millennial temperature changes at
715 high latitudes during the Last Interglacial, *Quat. Sci. Rev.*, 103, 116–133, doi:10.1016/j.quascirev.2014.08.018,
2014.



- Capron, E., Govin, A., Feng, R., Otto-Bliesner, B. L. and Wolff, E. W.: Critical evaluation of climate syntheses to benchmark CMIP6/PMIP4 127 ka Last Interglacial simulations in the high-latitude regions, *Quat. Sci. Rev.*, 168, 137–150, doi:10.1016/j.quascirev.2017.04.019, 2017.
- 720 Compo, G. P., Whitaker, J. S., Sardeshmukh, P. D., Matsui, N., Allan, R. J., Yin, X., Gleason, B. E., Vose, R. S., Rutledge, G., Bessemoulin, P., et al.: The twentieth century reanalysis project, *Quarterly Journal of the Royal Meteorological Society*, 137, 1–28, 2011.
- deMenocal, P., Ortiz, J., Guilderson, T., Adkins, J., Sarnthein, M., Baker, L., and Yarusinsky, M.: Abrupt onset and termination of the African Humid Period: rapid climate responses to gradual insolation forcing, *Quaternary Sci. Rev.*, 19, 347–361, 2000.
- 725 Dutton, A., Carlson, A. E., Long, A. J., Milne, G. A., Clark, P. U., DeConto, R., Horton, B. P., Rahmstorf, S., and Raymo, M. E.: Sea-level rise due to polar ice-sheet mass loss during past warm periods, *Science*, 349, <https://doi.org/10.1126/science.aaa4019>, 2015a.
- Dutton, A., Webster, J. M., Zwart, D., Lambeck, K., and Wohlfarth, B.: Tropical tales of polar ice: evidence of Last Interglacial polar ice sheet retreat recorded by fossil reefs of the granitic Seychelles islands, *Quaternary Sci. Rev.*, 107, 182–196, 2015b.
- 730 Eyring, V., S. Bony, G. A. Meehl, C. A. Senior, B. Stevens, R. J. Stouffer, and K. E. Taylor (2016), Overview of the Coupled Model Intercomparison Project phase 6 (CMIP6) experimental design and organization, *Geosci. Model Dev.*, 9, 1937–1958, doi: 10.5194/gmd-9-1937-2016, 2016.
- Folland, C. K., Karl, T. R., and Vinnikov, K. Y.: Observed climate variations and change, in: *Climate Change: The IPCC Scientific Assessment*, edited by: Houghton, J. T., Jenkins, G. J., and Ephraums, J., 195–238, Cambridge Univ. Press, New York, 1990.
- 735 Harrison, S. P., Bartlein, P. J., Izumi, K., Li, G., Annan, J., Hargreaves, J., Braconnot, P., and Kageyama, M.: Evaluation of CMIP5 palaeo-simulations to improve climate projections, *Nature Climate Change*, 5, 735–743, 2015.
- 740 Hoffman, J. S., Clark, P. U., Parnell, A. C. and He, F.: Regional and global sea-surface temperatures during the last interglaciation, *Science*, 355(6322), 276, doi:10.1126/science.aai8464, 2017.
- Holland, M. M., and C. M. Bitz 2003: Polar Amplification of Climate Models in coupled Models. *Climate Dynamics*, 21: 221–232 DOI 10.1007/s00382-003-0332-6, 2003.
- 745 Holloway, M.D., Sime, L.C., Allen, C.S., Hillenbrand, C.-D., Bunch, P., Wolff, E., Valdes, P.J.: The spatial structure of the 128 ka Antarctic sea ice minimum. *Geophysical Research Letters*, 44, 11129–11139, 2017.
- Holloway, M.D., Sime, L.C., Singarayer, J.S., Tindall, J.C., Valdes, P.J.: Simulating the 128 ka Antarctic climate response to Northern Hemisphere ice sheet melting using the isotope-enabled HadCM3. *Geophysical Research Letters*, 45, 11921–11929. 10.1029/2018GL079647, 2018
- 750 Ilyas, M., Brierley, C. M., and Guillas, S.: Uncertainty in regional temperatures inferred from sparse global observations: Application to a probabilistic classification of El Niño, *Geophysical Research Letters*, 44, 9068–9074, 2017.
- Jansen, E., Overpeck, J., Briffa, K. R., Duplessy, J. C., Joos, F., Masson-Delmotte, V., Olago, D., Otto-Bliesner, B., Peltier, W. R., Rahmstorf, S., Ramesh, R., Raynaud, D., Rind, D., Solomon, O., Villalba, R., and Zhang, D.: Palaeoclimate, in: *Climate Change 2007: The Physical Science Basis. Contribution of Working Group I to the Fourth Assessment Report of the Intergovernmental Panel on Climate Change*, edited by: Solomon, S., Qin, D., Manning, M., Chen, Z., Marquis, M., Averyt, K. B., Tignor, M., and Miller, H. L., Cambridge University Press, Cambridge, United Kingdom and New York, NY, USA, 2007.
- 755 Joussaume, S., Taylor, K., Braconnot, P., Mitchell, J., Kutzbach, J., Harrison, S., Prentice, I., Broccoli, A., Abe-Ouchi, A., Bartlein, P., et al.: Monsoon changes for 6000 years ago: results of 18 simulations from the Paleoclimate Modeling Intercomparison Project (PMIP), *Geophysical Research Letters*, 26, 859–862, 1999.
- 760 Kageyama, M. L. C. Sime, M. Sicard, M.-V. Guarino, A. de Vernal, D. Schroeder, R. Stein, I. Malmierca-Vallet, A. Abe-Ouchi, C. Bitz, P. Braconnot, E. Brady, M. A. Chamberlain, D. Feltham, C. Guo, G. Lohmann, K. Meissner, L. Menviel, P. Morozova, K. H. Nisancioglu, B. Otto-Bliesner, R. Oishi, S. Sherriff-Tadano, J.



- 765 Stroeve, X. Shi, B. Sun, E. Volodin, N. Yeung, Q. Zhang, Z. Zhang, and T. Ziehn: A multi-model CMIP6 study of Arctic sea ice at 127 ka: Sea ice data compilation and model differences, submitted to *Climates of the Past*, 2019.
- Kim S-J, Lü JM, Yi S, Choi T, Kim B-M, Lee BY, *et al.* Climate response over Asia/Arctic to change in orbital parameters for the last interglacial maximum. *Geosciences Journal* 2010, **14**(2): 173-190.
- Kohfeld, K. and Harrison, S. P.: How well can we simulate past climates? Evaluating the models using global palaeoenvironmental datasets, *Quaternary Sci. Rev.*, 19, 321–346, 2000.
- 770 Kutzbach, J. E. and B. L. Otto-Bliesner: The sensitivity of the African-Asian monsoonal climate to orbital parameter changes for 9000 yr B.P. in a low-resolution general circulation model. *J. Atmos. Sci.*, 39, 1177-1188, 1982.
- Larrasoaña, J. C., Roberts, A. P. & Rohling, E. J.: Dynamics of Green Sahara periods and their role in hominin evolution, *PLoS ONE* 8, e76514, 2013.
- Levis, S., G.B. Bonan, and C. Bonfils: Soil feedback drives the mid-Holocene North African monsoon northward in fully coupled CCSM2 simulations with a dynamic vegetation model, *Clim. Dyn.*, 23, 791-802, 2004.
- LIGA members: The last interglacial in high latitudes of the Northern Hemisphere: Terrestrial and marine evidence, *Quatern. Int.*, 10–12, 9–28, 1991.
- Lisiecki, L. E., and Raymo, M. E. (2009), Diachronous benthic $\delta^{18}\text{O}$ responses during late Pleistocene terminations, *Paleoceanography*, 24, PA3210, doi:[10.1029/2009PA001732](https://doi.org/10.1029/2009PA001732).
- 780 Lunt, D. J., Abe-Ouchi, A., Bakker, P., Berger, A., Braconnot, P., Charbit, S., Fischer, N., Herold, N., JungCLAUS, J. H., Khon, V. C., Krebs-Kanzow, U., Langebroeck, P. M., Lohmann, G., Nisan-cioglu, K. H., Otto-Bliesner, B. L., Park, W., Pfeiffer, M., Phipps, S. J., Prange, M., Rachmayani, R., Renssen, H., Rosenbloom, N., Schneider, B., Stone, E. J., Takahashi, K., Wei, W., Yin, Q., and Zhang, Z. S.: A multi-model assessment of last interglacial temperatures, *Clim. Past*, 9, 699–717, <https://doi.org/10.5194/cp-9-699-2013>, 2013.
- 785 Marino, G., Rohling, E. J., Rodriguez-Sanz, L., Grant, K. M., Heslop, D., Roberts, A. P., Stanford, J. D., and Yu, J.: Bipolar seesaw control on last interglacial sea level, *Nature*, 980 522, 197–+, 2015.
- Masson-Delmotte, V., Kageyama, M., Braconnot, P., Charbit, S., Krinner, G., Ritz, C., Guilyardi, E., Jouzel, J., Abe-Ouchi, A., Crucifix, M., Gladstone, R. M., Hewitt, C. D., Kitoh, A., LeGrande, A. N., Marti, O., Merkel, U., Motoi, T., Ohgaito, R., Otto-Bliesner, B., Peltier, W. R., Ross, I., Valdes, P. J., Vettoretti, G., Weber, S.
- 790 L., Wolk, F., and Yu, Y.: Past and future polar amplification of climate change: climate model intercomparisons and ice-core constraints, *Clim. Dynam.*, 26, 513–529, 2006.
- Masson-Delmotte, V., Stenni, B., Blunier, T., Cattani, O., Chappellaz, J., Cheng, H., Dreyfus, G., Edwards, R. L., Falourd, S., Govin, A., Kawamura, K., Johnsen, S. J., Jouzel, J., Landais, A., Lemieux-Dudon, B., Laurantou, A., Marshall, G., Minster, B., Mudelsee, M., Pol, K., Rothlisberger, R., Selmo, E., and Waelbroeck, C.: Abrupt change of Antarctic moisture origin at the end of Termination II, *P. Natl. Acad. Sci. USA*, 107, 12091–12094, 2010.
- 795 Masson-Delmotte, V., Schulz, M., Abe-Ouchi, A., Beer, J., Ganopolski, A., Gonzalez Rouco, J., Jansen, E., Lambeck, K., Luterbacher, J., Naish, T., Osborn, T., Otto-Bliesner, B., Quinn, T., Ramesh, R., Rojas, M., Shao, X., and Timmermann, A.: Information from paleoclimate archives, in: *The Physical Science Basis. Contribution of Working Group I to the Fifth Assessment Report of the Intergovernmental Panel on Climate Change*, edited by: Stocker, T. F., Qin, D., Plattner, G.-K., Tignor, M., Allen, S. K., Boschung, J., Nauels, A., Xia, Y., Bex, V., and Midgley, P. M., Cambridge University Press, Cambridge, United Kingdom and New York, NY, USA, 2013.
- Melles M, Brigham-Grette J, Minyuk PS, Nowaczyk NR, Wennrich V, DeConto RM, Anderson PM, Andreev AA, Coletti A, Cook TL, Haltia-Hovi E, Kukkonen M, Lozhkin AV, Rosén P, Tarasov P, Vogel H, Wagner B.: 2.8 million years of Arctic climate change from Lake El'gygytyn, NE Russia, *Science* 337(6092), 315-320; doi: [10.1126/science.1222135](https://doi.org/10.1126/science.1222135), 2012.
- 805 Morice, C. P., Kennedy, J. J., Rayner, N. A., and Jones, P. D.: Quantifying uncertainties in global and regional temperature change using an ensemble of observational estimates: The HadCRUT4 data set, *Journal of Geophysical Research: Atmospheres*, 117, 2012.
- 810 Nowicki, S. M. J., Payne, A., Larour, E., Seroussi, H., Goelzer, H., Lipscomb, W., Gregory, J., Abe-Ouchi, A., and Shepherd, A.: Ice Sheet Model Intercomparison Project (ISMIP6) contribution to CMIP6, *Geosci. Model Dev.*, 9, 4521–4545, <https://doi.org/10.5194/gmd-9-4521-2016>, 2016.



- 815 Otto-Bliesner, B. L., Rosenbloom, N., Stone, E. J., McKay, N. P., Lunt, D. J., Brady, E. C., and Overpeck, J. T.: How warm was the last interglacial? New model-data comparisons, *Philos. T. R. Soc. A*, 371, 2001, <https://doi.org/10.1098/rsta.2013.0097>, 2013.
- Otto-Bliesner, B. L., Braconnot, P., Harrison, S. P., Lunt, D. J., Abe-Ouchi, A., Albani, S., Bartlein, P. J., Capron, E., Carlson, A. E., Dutton, A., et al.: The PMIP4 contribution to CMIP6–Part 2: Two interglacials, scientific objective and experimental design for Holocene and Last Interglacial simulations, *Geoscientific Model Development*, 10, 3979–4003, 2017.
- 820 Pausata, F. S. R., Messori, G., and Zhang, Q.: Impacts of dust reduction on the northward expansion of the African monsoon during the Green Sahara period, *Earth Planet. Sci. Lett.*, 434, 298–307, 2016.
- Rayner, N. A., Parker, D. E., Horton, E. B., Folland, C. K., Alexander, L. V., Rowell, D. P., Kent, E. C. and Kaplan, A.: Global analyses of sea surface temperature, sea ice, and night marine air temperature since the late nineteenth century, *J. Geophys. Res. Atmospheres*, 108(D14), 4407, doi:10.1029/2002JD002670, 2003.
- 825 Salonen, J.S., Helmens, K.F., Brendryen, J. *et al.* Abrupt high-latitude climate events and decoupled seasonal trends during the Eemian. *Nat Commun* 9, 2851 doi:10.1038/s41467-018-05314-1, 2018.
- Sánchez Goñi, M.F., Landais, A., Fletcher, W.J., Naughton, F., Desprat, S. & Duprat, J.: Contrasting impacts of Dansgaard–Oeschger events over a western European latitudinal transect modulated by orbital parameters, *Quat. Sci. Rev.*, 27, 1136–1151, 2008.
- 830 Schmidt, G. A., Annan, J. D., Bartlein, P. J., Cook, B. I., Guilyardi, E., Hargreaves, J. C., Harrison, S. P., Kageyama, M., LeGrande, A. N., Konecky, B., Lovejoy, S., Mann, M. E., Masson-Delmotte, V., Risi, C., Thompson, D., Timmermann, A., Tremblay, L.-B., and Yiou, P.: Using palaeo-climate comparisons to constrain future projections in CMIP5, *Clim. Past*, 10, 221–250, <https://doi.org/10.5194/cp-10-221-2014>, 2014.
- Scussolini, P., et al.: Agreement between reconstructed and modeled boreal precipitation of the Last Interglacial, *Science Advances*, 5, eaas7047, 2019.
- 835 Shackleton, N. J., Sánchez Goñi, M. F., Pailler, D. & Lancelot, Y.: Marine isotope substage 5e and the Eemian Interglacial, *Glob. Planet. Change*, 757, 1–5, 2003.
- Stone, E. J., Capron, E., Lunt, D. J., Payne, T. J., Singarayer, J. S., Valdes, P. J., and Wolff, E. W.: Impact of meltwater on high-latitude early Last Interglacial climate, *Clim. Past*, 12, 1919–1932, 2016.
- 840 Swann, A.L., I.Y. Fung, S. Levis, G.B. Bonab, and S.C. Doney: Changes in Arctic vegetation amplify high-latitude warming through the greenhouse effect, *PNAS*, 107, 1295–1300, 2010.
- Stein, R., Fahl, K., Gierz, P., Niessen, F., and Lohmann, G.: Arctic Ocean sea ice cover during the penultimate glacial and the last interglacial, *Nature communications*, 8, <https://doi.org/10.1038/s41467-017-00552-1>, 2017.
- Turney, C. S. M., R. T. Jones, Does the Agulhas Current amplify global temperatures during super-interglacials? *J. Quat. Sci.* 25, 839–843, 2010.
- 845 Tzedakis, P.C.: Last Interglacial pollen records from Europe. In: Elias, S.A. (ed.) *Encyclopaedia of Quaternary Science*, pp 2597–2605 (Elsevier, Amsterdam, 2007).
- Tzedakis, P.C., Raynaud, D.R., McManus, J.F., Berger, A., Brovkin, V. & Kiefer, T.: Interglacial diversity. *Nature Geoscience* 2, 751–755, 2009.
- 850 Velichko, A. A., Borisova, O. K. & Zelikson, E. M.: Paradoxes of the Last Interglacial climate: reconstruction of the northern Eurasia climate based on palaeofloristic data. *Boreas*, Vol. 37, pp. 1–19. 10.1111/j. 1502-3885.2007.00001.x. ISSN 0300-9483, 2008.
- Veres, D., Bazin, L., Landais, A., Toyé Mahamadou Kele, H., Lemieux-Dudon, B., Parrenin, F., Martinerie, P., Blayo, E., Blunier, T., Capron, E., Chappellaz, J., Rasmussen, S. O., Severi, M., Svensson, A., Vinther, B. and Wolff, E. W.: The Antarctic ice core chronology (AICC2012): an optimized multi-parameter and multi-site dating approach for the last 120 thousand years, *Clim Past*, 9(4), 1733–1748, doi:10.5194/cp-9-1733-2013, 2013.
- 855 Wang, B., Kim, H.-J., Kikuchi, K., and Kitoh, A.: Diagnostic metrics for evaluation of annual and diurnal cycles, *Climate Dynamics*, 37, 941–955, 2011.
- Yin, Q. Z. and Berger, A.: Individual contribution of insolation and CO₂ to the interglacial climates of the past 800, 860 000 years, *Clim. Dynam.*, 38, 709–724, <https://doi.org/10.1007/s00382-011-1013-5>, 2012.

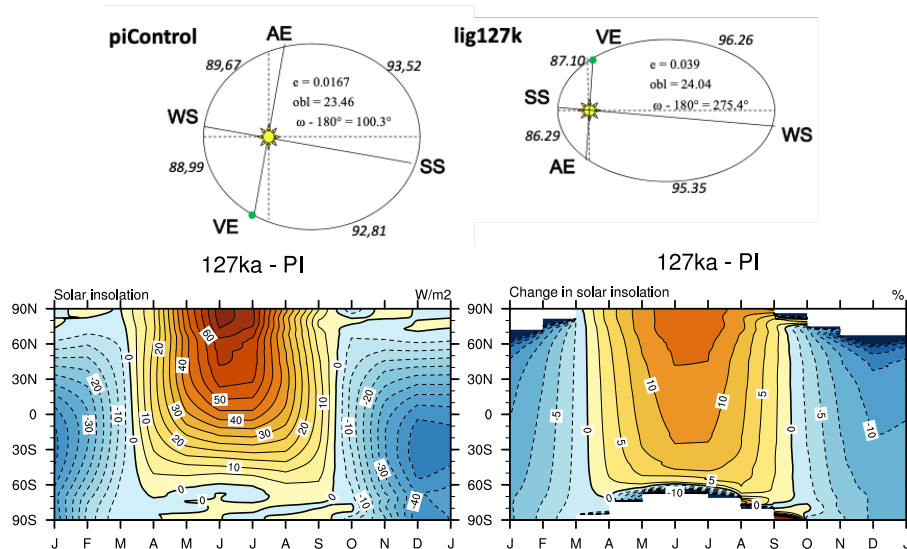


Figure 1. (top) Orbital configurations for the *piControl* and *lig127k* experiments. The number of days between the vernal equinox and summer solstice, summer solstice and autumnal equinox, etc are indicated along the periphery of the ellipse. (bottom) Latitude-month insolation anomalies 127 ka – 1850 in (left) Watts/m² and (right) percentage change from PI.

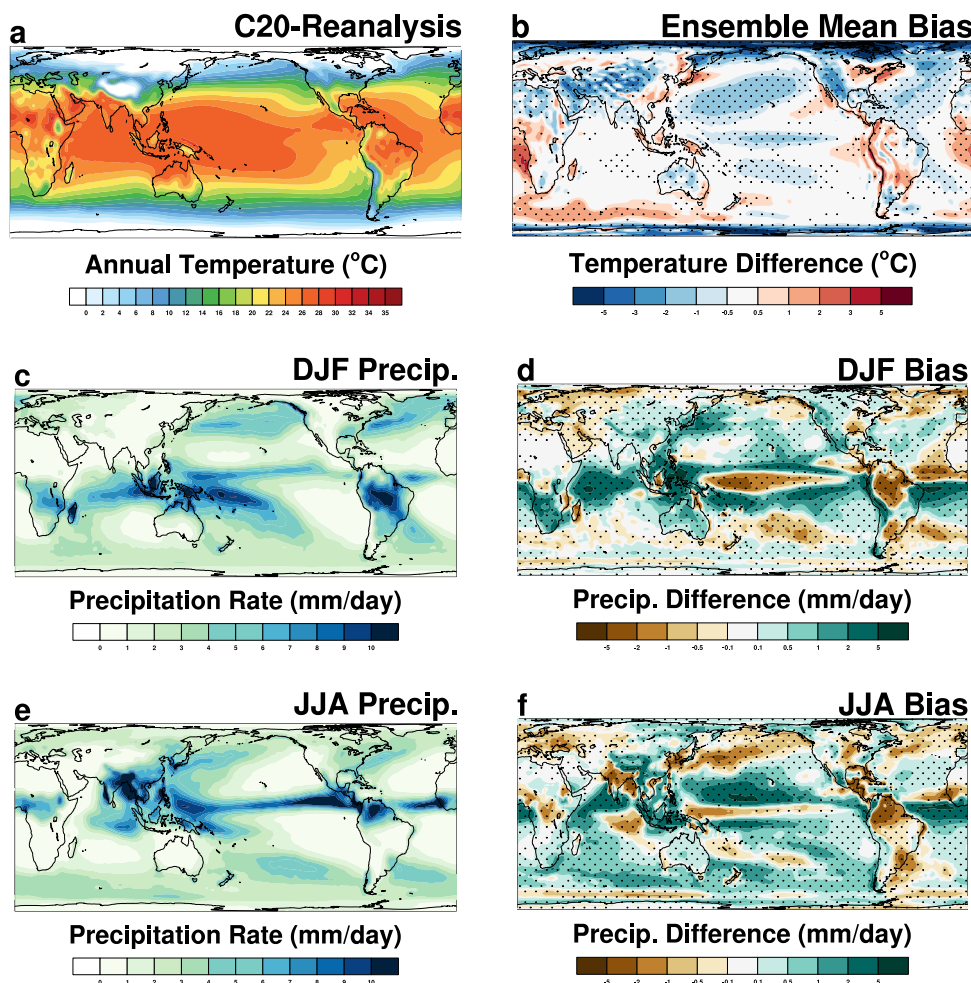


Figure 2. Comparison of the CMIP6 ensemble to observations. (a) The annual mean surface temperatures in the C20 Reanalysis (Compo et al., 2011) between 1871-1900. (b) The ensemble mean difference in annual surface air temperature from the C20 Reanalysis within the preindustrial control simulations. Ability of the ensemble to simulate the seasonal cycle of precipitation for the present-day. (c,e) The precipitation climatology seen in the GPCP (Adler et al., 2003) observational dataset between 1971-2000 for DJF and JJA respectively. (d,f) The ensemble mean difference in seasonal precipitation from GPCP within the preindustrial control simulations for DJF and JJA respectively. Stippling indicates that two-thirds of the models agree on the sign of the bias.

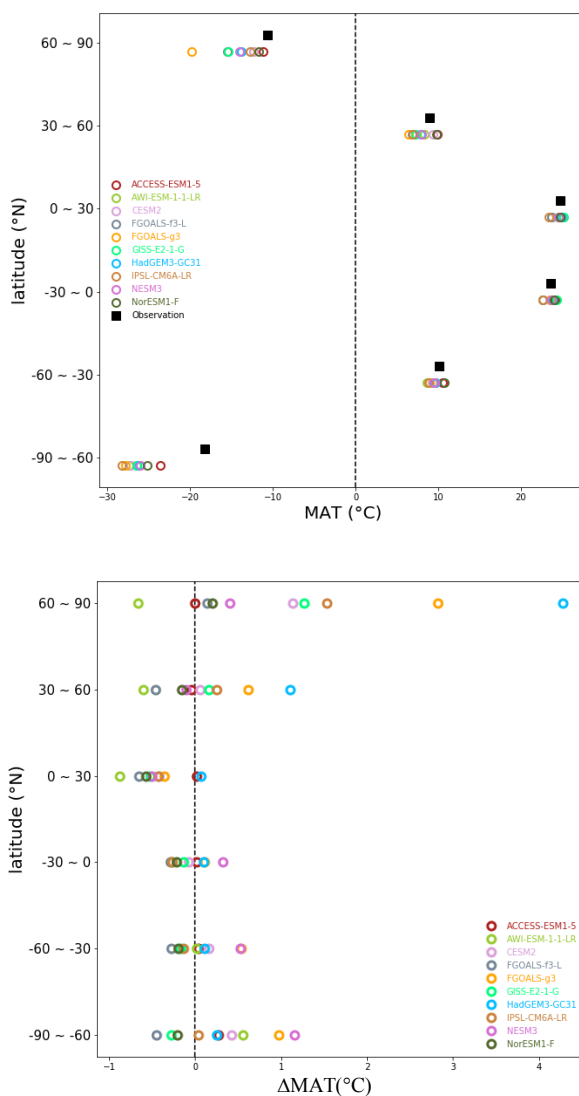


Figure 3. (top) Comparison of the preindustrial zonal mean temperature profile of individual climate models to the 1850-1900 observations. The area-averaged, annual mean surface air temperature for 30° latitude bands in the CMIP6 models and a spatially complete compilation of instrumental observations over 1850-1900 (black, Ilyas et al., 2017; Morice et al., 2012). (bottom) Changes in latitudinal temperature gradients (*lig127k* minus *piControl*). The simulated annual mean temperature change in averaged over broad zonal bands is presented for each of the individual CMIP6 models.

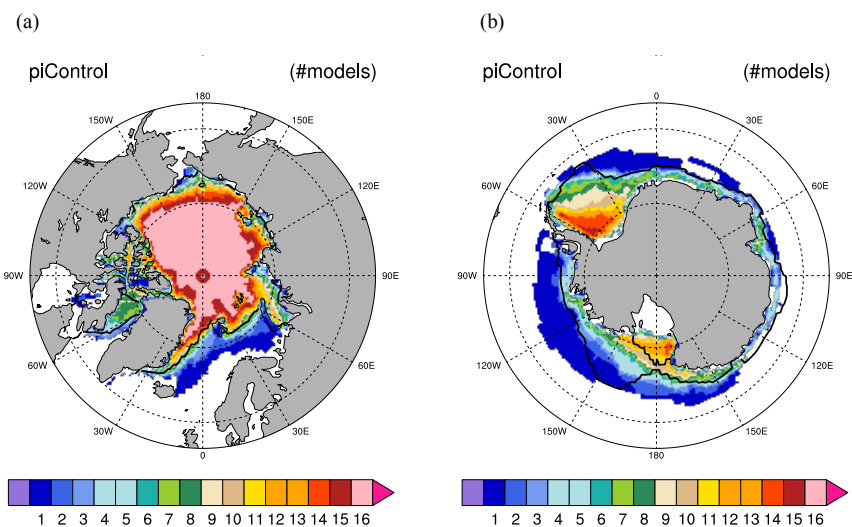


Figure 4. Comparison of the *piControl* sea ice distributions in the Northern Hemisphere for August-September (left) and in the Southern Hemisphere for February-March (right). For each $1^\circ \times 1^\circ$ longitude-latitude grid cell, the figure indicates the number of models that simulate at least 15% of the area covered by sea ice. The observed 15% concentration boundaries (black lines) are the 1870-1899 CE interval based on the Hadley Centre Sea Ice and Sea Surface Temperature (HadISST; Rayner et al., 2003) data set. See Figure S1 for individual model results.

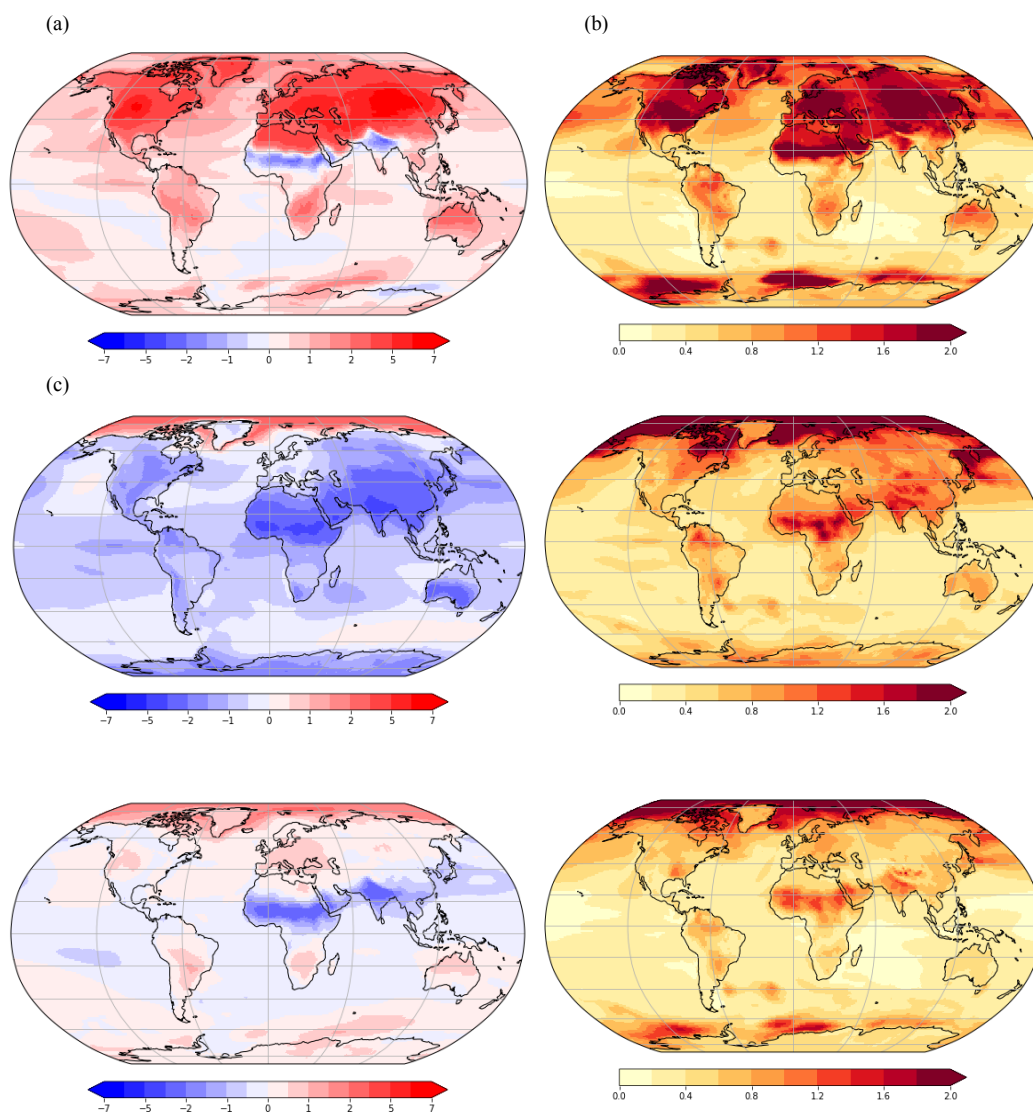


Figure 5. Multi-model ensemble average changes (left) and standard deviations of ensemble changes (right) of surface air temperatures ($^{\circ}\text{C}$) for *lig127k* minus *piControl*. Shown are June-July-August (top), December-January-February (middle), and Annual mean (bottom) changes.

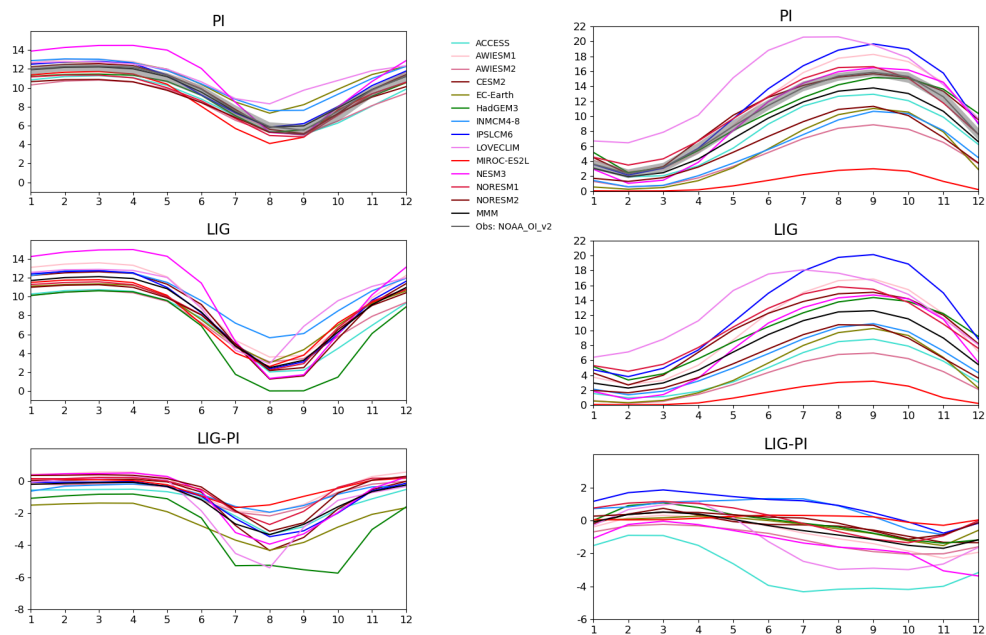


Figure 6. The simulated Arctic (left) and Antarctic (right) annual cycle of area of sea ice greater than 15% (10^6 km^2) for the (a, top) PI and (b, bottom) LIG

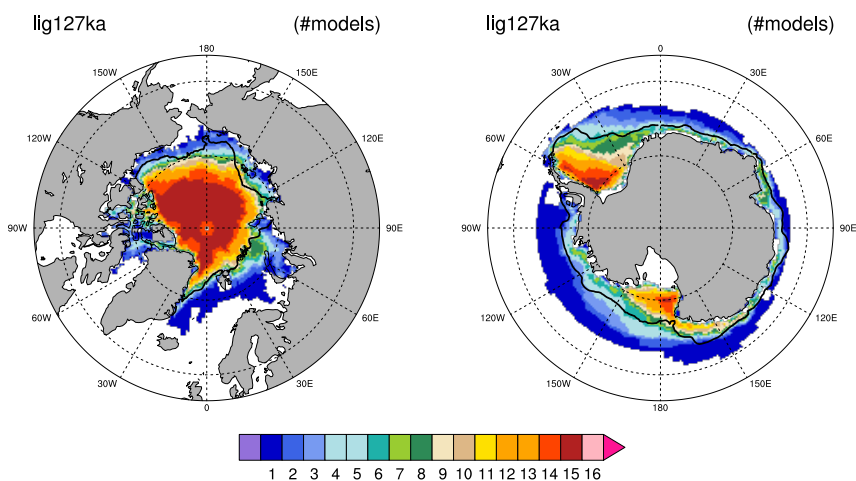


Figure 7. Comparison of the *lig127k* sea ice distributions in the Northern Hemisphere for August-September (left) and in the Southern Hemisphere for February-March (right). For each 1° x 1° longitude-latitude grid cell, the figure indicates the number of models that simulate at least 15% of the area covered by sea ice. The average 15% concentration boundaries (black lines) are average for 2000-2018. See Figure S1 for individual model results.

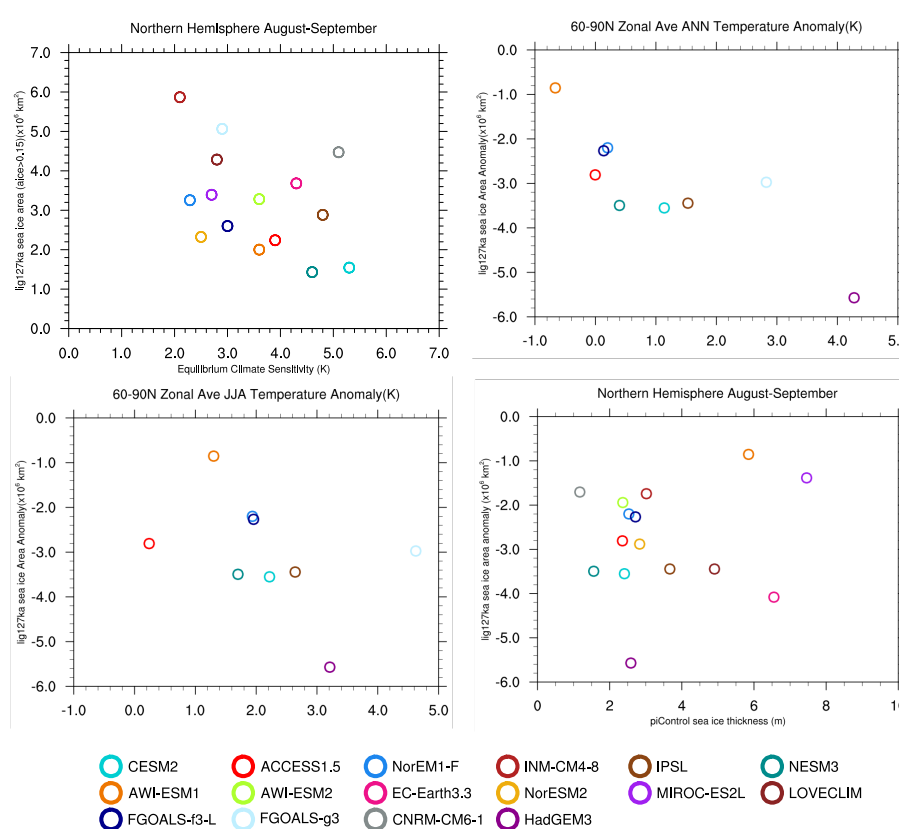


Figure 8. (top, left) lig127k August-September sea ice area (10^6 km^2) versus Equilibrium Climate Sensitivity (ECS, K); (top, right) lig127k August-September sea ice area anomaly (10^6 km^2) versus lig127k annual 60-90°N surface air temperature anomaly ($^{\circ}\text{C}$); (bottom, left) lig127k August-September sea ice area anomaly (10^6 km^2) versus lig127k JJA 60-90°N surface air temperature anomaly ($^{\circ}\text{C}$); and (bottom, right) lig127k August-September sea ice area anomaly (10^6 km^2) versus piControl sea ice thickness (m).

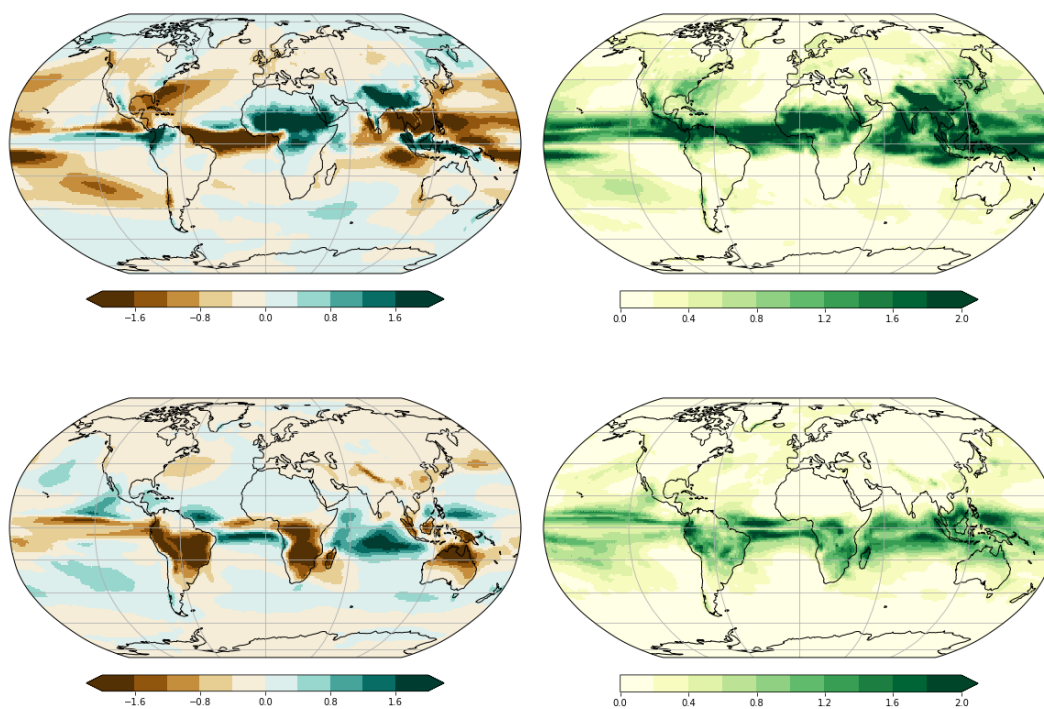


Figure 9. Multi-model ensemble average changes (left) and standard deviations of ensemble changes (right) of precipitation (mm/day) for *lig127k* minus *piControl*. Shown are June-July-August (top), December-January-February (bottom) changes.

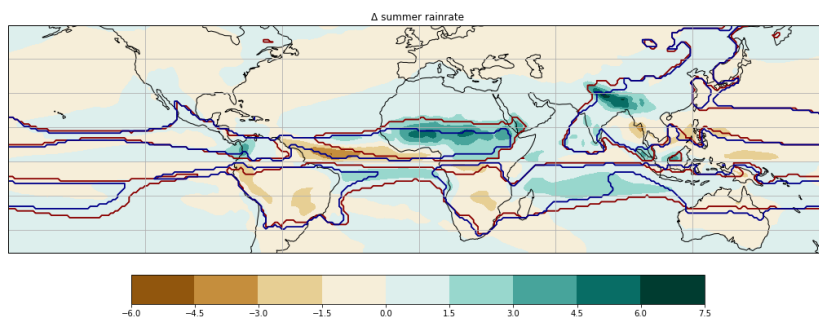


Figure 10. Ensemble-averaged Last Interglacial change in monsoon-related rainfall rate (in mm/day). Red and blue contours show the boundaries of *lig127k* and *piControl* monsoon domains, respectively, using the definitions of Wang et al. (2011).

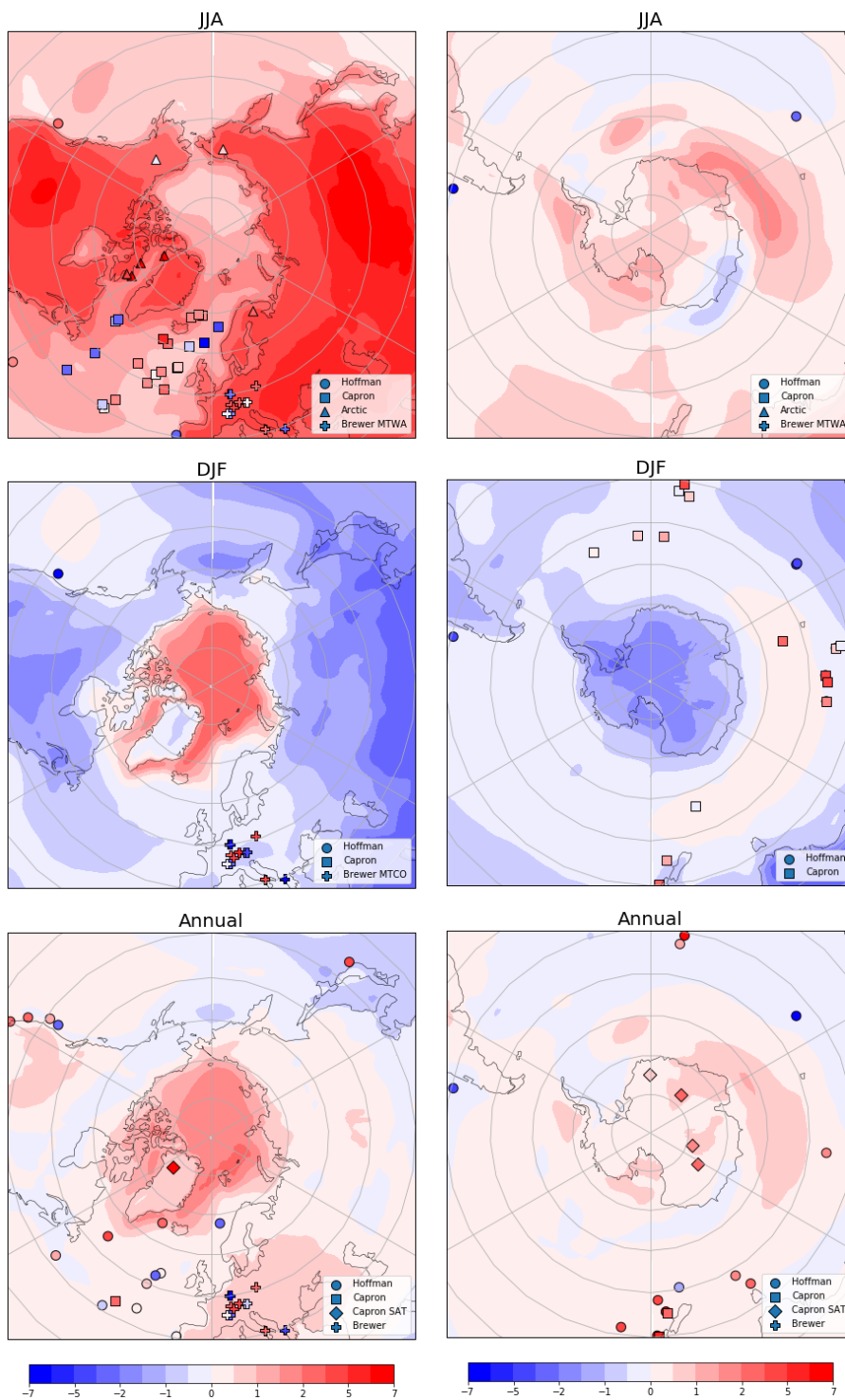




Figure 11. High-latitude surface temperature anomaly between 127 ka and Preindustrial from models (ensemble average in contoured colors) and proxies (filled markers : dots for the compilation by Hoffman et al. 2017, squares and diamonds for marines sites and ice cores, respectively, of the compilation by Capron et al. 2014, 2017). (top) June-July-August, (middle) December-January-February, (bottom) Annual. The preindustrial reference is 1850 CE for model anomalies and for the data is 1870-1899 for Capron, and 1870-1889 for Hoffman.

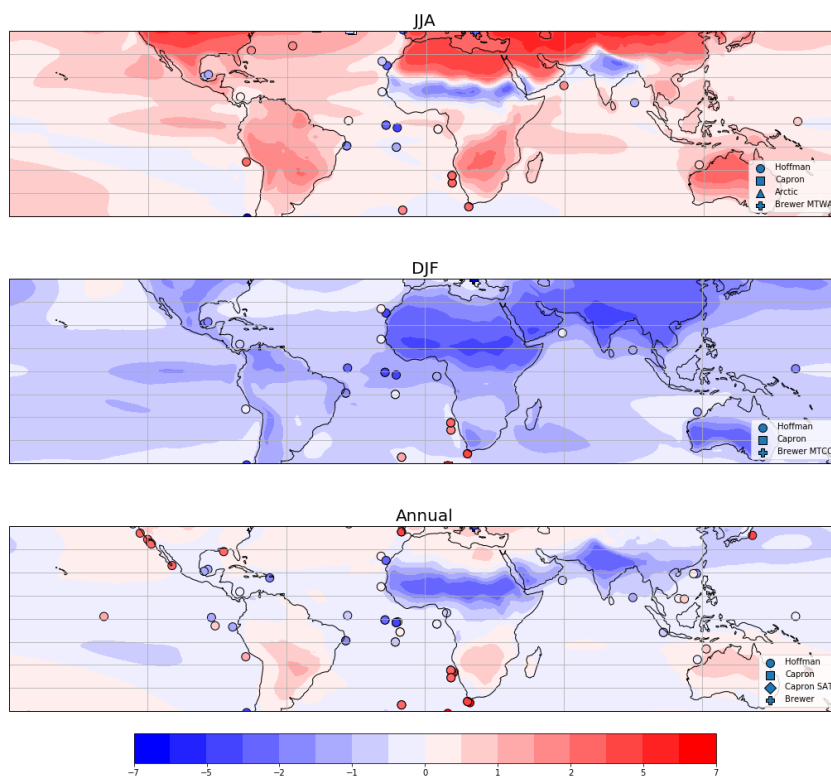


Figure 12. Same as Figure 11 but for low-latitude (40°S – 40°N) surface temperature.

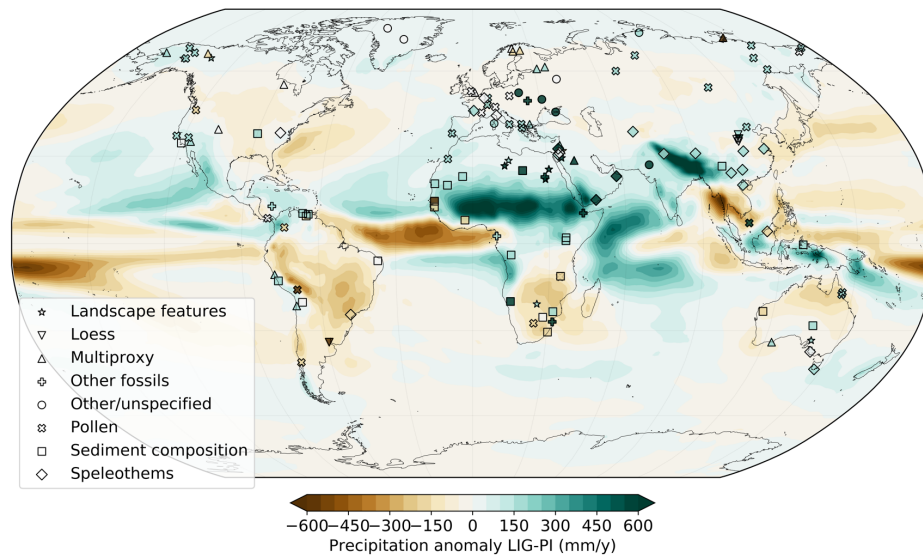


Figure 13. Annual precipitation anomaly between 127 ka and Preindustrial simulations (ensemble average in contoured colors) and proxies (filled markers). Green colors indicate higher precipitation during the LIG from models or proxies and conversely for brown colors. Proxy anomalies are on a semiquantitative scale: dark blue (much wetter LIG), light blue (wetter), white (no noticeable anomaly), light red (drier), and dark red (much drier). Different markers represent different types of proxy records. Proxy reconstruction from Scussolini et al., 2019.

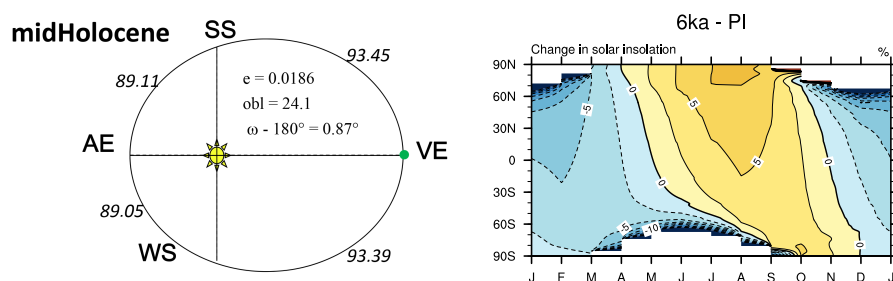


Figure 14. (left) Orbital configuration for the *midHolocene* (6ka) experiment. (right) Latitude-month insolation anomalies 6 ka–1850 as percentage change from PI.

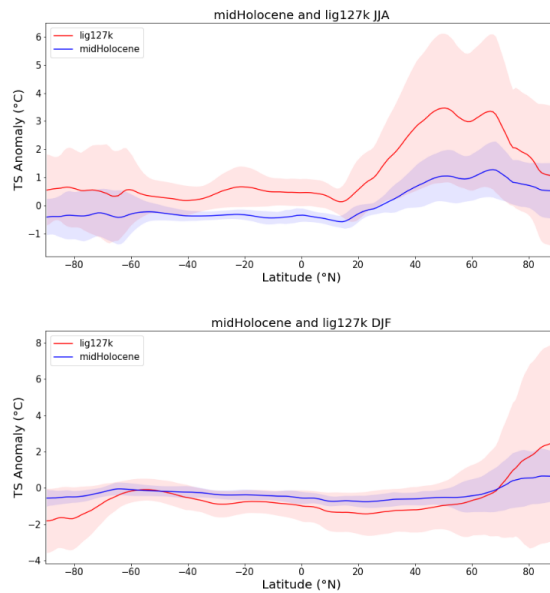


Figure 15. Multi-model ensemble mean and two standard deviation, zonal surface air temperature anomalies for *midHolocene* and *lig127k* simulations for JJA and DJF (see Brierley et al., 2019 for more details on *midHolocene* simulations).

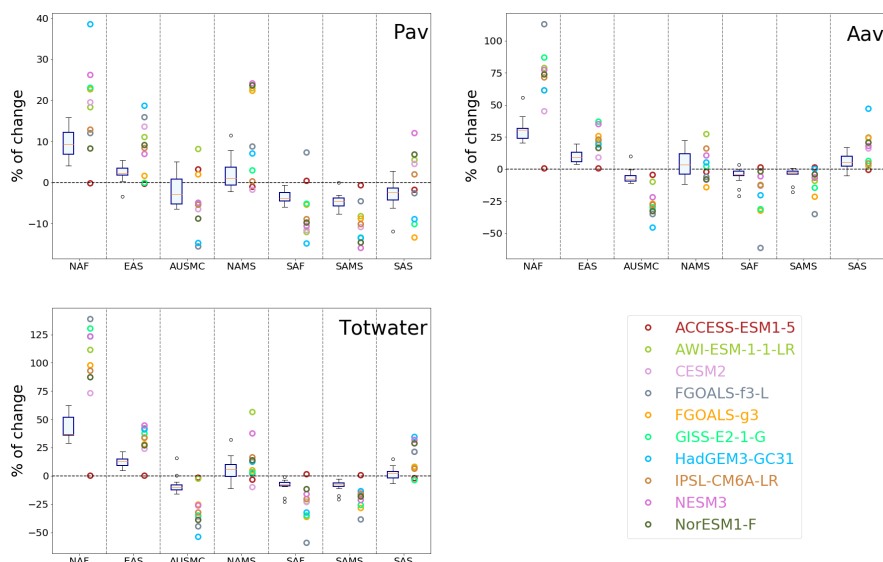


Figure 16. Relative changes in individual *lig127k* monsoons. Three different monsoon diagnostics as computed for each of seven different regional domains for the individual CMIP6 *lig127k* simulations. The comparable results from the *midHolocene* simulations are shown with boxes and whiskers (for details see Brierley et al., 2019). (Pav) The percentage changes in area-averaged precipitation rate during the monsoon season. (Aav) The percentage change in the areal extent of the regional monsoon domain. (Totwater) The percentage change in the total amount of water precipitated in each monsoon domain season (computed as the precipitation rate multiplied by the areal extent). The abbreviations used to identify each regional domain are: North America Monsoon System (NAMS), North Africa (NAF), Southern Asia (SAS) and East Asia (EAS) in the Northern Hemisphere and South America Monsoon System (SAMS), South Africa (SAF) and Australian-Maritime Continent (AUSMC) in the Southern Hemisphere.

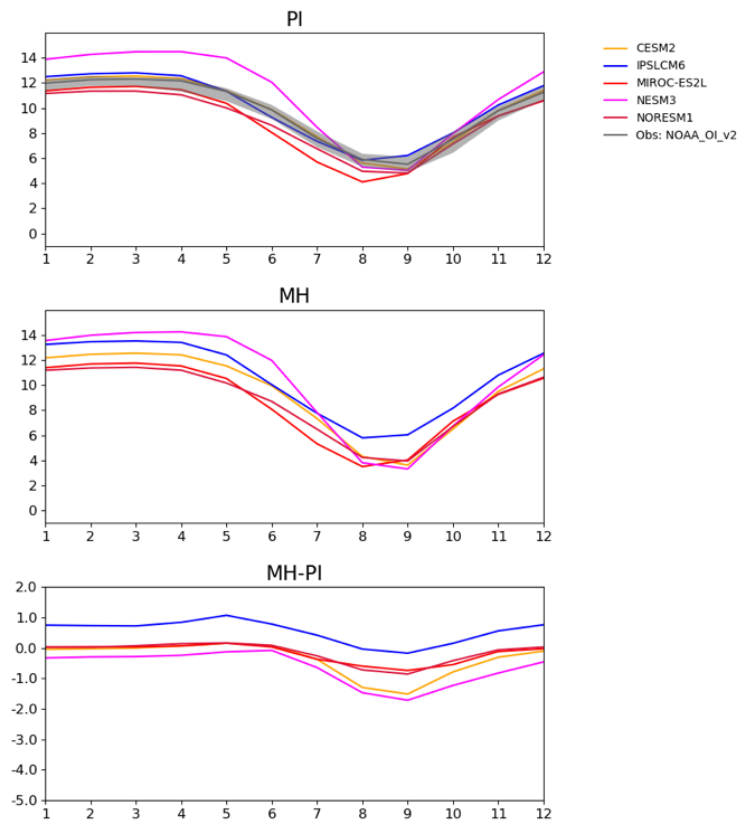


Figure 17. The Arctic annual cycle of area of sea ice greater than 15% (10^6 km²) for the (a, top) PI, (b, bottom) MH for a subset of the models.



Table 1. Protocols: forcings and boundary conditions

	1850 C.E. (DECK <i>piControl</i>)	127ka (<i>lig127k</i>)
Orbital parameters¹		
Eccentricity	0.016764	0.039378
Obliquity (degrees)	23.459	24.040
Perihelion - 180	100.33	275.41
Vernal equinox	Fixed to noon on March 21	Fixed to noon on March 21
Greenhouse gases		
Carbon dioxide (ppm)	284.3	275
Methane (ppb)	808.2	685
Nitrous oxide (ppb)	273.0	255
Other GHG gases	CMIP DECK <i>piControl</i>	0
Solar constant (Wm ⁻²)	TSI: 1360.747	Same as <i>piControl</i>
Paleogeography	Modern	Same as <i>piControl</i>
Ice sheets	Modern	Same as <i>piControl</i>
Vegetation	CMIP DECK <i>piControl</i>	Prescribed or interactive as in <i>piControl</i>
Aerosols Dust, Volcanic, etc.	CMIP DECK <i>piControl</i>	Prescribed or interactive as in <i>piControl</i>

¹The term ‘orbital parameters’ is used to denote the variations in the Earth’s eccentricity and longitude of perihelion as well as changes in its axial tilt (obliquity).



Table 2. Summary of models in this intercomparison [note not all models yet included in all figures]

Climate Model	Institution Name	Citation for Model Description	Equilibrium Climate Sensitivity	Experimental Protocol Comments
			MIP	
ACCESS1.5 (ACCESS ESM 1.5)	UNSW and CSIRO	Ziehn et al., GMD, 2017 and Ziehn et al., in preparation	3.9°C CMIP6 PMIP4	Fixed vegetation with interactive LAI, Prescribed aerosols; SC=1365.65 W/m ²
CESM2 (CESM2.1)	NCAR	Danabasoglu et al. JAMES, 2019	5.3°C CMIP6 PMIP4	Crops and Urban areas removed; Prescribed potential vegetation with interactive LAI, Simulated dust
EC-Earth3 (EC-Earth3-LR, version 3.3)	Stockholm University	Doescher and the EC-Earth Consortium, in preparation, 2019	4.3°C CMIP6 PMIP4	Prescribed vegetation and aerosols
HadGEM3 (HadGEM3-GC3.1, N96 ORCA1 version)	BAS	Walters. et al. GMD, 2019 Williams, K. D., et al., JAMES, 2018.	— CMIP6 PMIP4	Prescribed vegetation and aerosols
INM-CM4-8	INM RAS	Volodin et al., Russian Journal of Numerical Analysis and Mathematical Modelling, 2018	2.1°C CMIP6 PMIP4	Prescribed vegetation, simulated aerosols
LOVECLIM (LOVECLIM, version 1.2)	UNSW	Goosse et al., GMD, 2010	2.8°C	Interactive vegetation
MIROC-ES2L	AORI University of Tokyo	Hajima et al., GMDD, 2019	2.7°C CMIP6 PMIP4	Prescribed vegetation and aerosols
NorESM1-F	Norwegian Climate Centre, NCC	Guo et al., GMD, 2019	2.29°C PMIP4	Prescribed vegetation and aerosols as PI
NorESM2 (NorESM2-LM)	Norwegian Climate Centre, NCC	—	2.5°C CMIP6 PMIP4	Prescribed vegetation and aerosols as PI
AWI-ESM1	AWI	Sidorenko, Dmitry, et al., Climate Dynamics, 2019	3.6°C CMIP6 PMIP4	Interactive vegetation
AWI-ESM2	AWI	—	3.6°C CMIP6 PMIP4	Interactive vegetation, prescribed aerosols
FGOALS-f3-L	CAS	He et al., 2020	3.3°C CMIP6 PMIP4	—
FGOALS-g3	CAS	Wang H., L. J. Li, X. L. Chen, B. Wang, 2020	2.8°C CMIP6 PMIP4	—



GISS-E2-1-G	NASA-GISS	Bauer and Tsigardis (2020)	2.7°C	—
			CMIP6 PMIP4	
IPSL-CM6A-LR	IPSL	Boucher, et al. (2020)	4.8°C	Prescribed vegetation, interactive phenology, prescribed PI aerosols
			CMIP6 PMIP4	
NESM3	NUIST	Cao et al. (2018)	4.6°C	—
			CMIP6 PMIP4	
CNRM-CM6-1	CNRM-CERFACS	—	5.1°C	—
			CMIP6 PMIP4	